Chapter 1
Precise Matter and Antimatter Tests of the Standard Model with e^-, e^+, p, $\overline{\mathrm{p}}$ and $\overline{\mathrm{H}}$

G. Gabrielse, S. Fogwell Hoogerheide, J. Dorr and E. Novitski

Abstract Extremely precise tests of the Standard Model of particle physics and its CPT theorem come from low energy measurements of the electron, positron, proton and antiproton magnetic moments and charge-to-mass ratios. Ground state antihydrogen atoms are now available for measurements that could eventually reach a higher precision, though no precise $\overline{\mathrm{H}}$ measurements have yet been carried out. After a brief summary of the results and status of such measurements, the focus is upon the most precisely measured and precisely calculated property of an elementary particle. The electron magnetic moment, measured to 3 parts in 10^{13}, is a probe of the interaction of the electron with the fluctuating vacuum described by quantum electrodynamics (QED). It is also a probe for electron substructure not predicted by the Standard Model. The measured magnetic moment, together with fine structure constant determined by a different method, is the most stringent test of QED and the Standard Model of particle physics. The measured magnetic moment and QED theory together yield the most precise measured value of the fine structure constant. The summary includes the antiproton magnetic moment that was recently measured precisely for the first time. The 4 parts in 10^6 precision is much less than the electron precision or the 9 parts in 10^{11} at which the antiproton and proton charge-to-mass ratios have been compared, but very large increases in precision seem possible as quantum methods are incorporated.

1.1 Overview Summary

Electron Magnetic Moment

The most precisely measured property of an elementary particle is the electron magnetic moment, measured in Bohr magnetons,

---

G. Gabrielse (✉) · S. Fogwell Hoogerheide · J. Dorr · E. Novitski
Department of Physics, Harvard University, 17 Oxford Street, Cambridge, MA 02138, USA
e-mail: gabrielse@physics.harvard.edu

W. Quint and M. Vogel (eds.), *Fundamental Physics in Particle Traps*,
Springer Tracts in Modern Physics 256, DOI: 10.1007/978-3-642-45201-7_1,

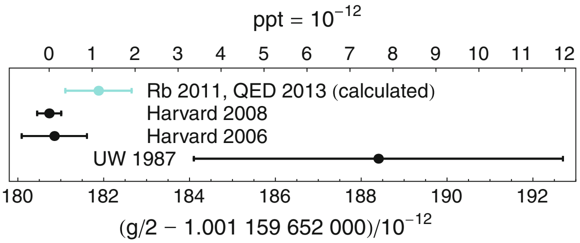

Fig. 1.1 The electron magnetic moment in Bohr magnetons, $\mu/\mu_B = -g/2$, is the most precisely measured property of an elementary particle. The good agreement of the measurement and the prediction of the Standard Model of particle physics is a great triumph of the Standard Model and QED

$$\mu/\mu_B = -g/2 = -1.001\,159\,652\,180\,73\,(28) \quad [0.28\text{ ppt}]. \tag{1.1}$$

A negative μ indicates that the magnetic moment $\boldsymbol{\mu}$ points opposite to the spin $\mathbf{S}$, with $\boldsymbol{\mu} = \mu\hat{\mathbf{S}}$ and $\hat{\mathbf{S}} = \mathbf{S}/(\hbar/2)$. The distinguishing feature of our Harvard measurements was using quantum jump spectroscopy of the lowest cyclotron states and spin states of a single electron bound to a cylindrical Penning trap apparatus [1–3]. Cooling to the lowest quantum states makes possible a much higher accuracy than realized in a long history of applying new methods to measuring the electron magnetic moment [4]. Our quantum measurements superseded the UW result that had stood for about 20 years [5], with an uncertainty 15 times lower and a measured value shifted by 1.7 standard deviations (Fig. 1.1). The new methods that made possible this large increase in precision are summarized in following sections.

Triumph of the Standard Model

Calculations based upon the Standard Model of particle physics relate the electron magnetic moment in Bohr magnetons to the fine structure constant α. Since the electron magnetic moment was measured, there has been impressive progress in the calculations [6] (reviewed in this volume by M. Hayakawa) and an improved determination of α that is independent of our electron magnetic moment measurement [7]. Together these predict a magnetic moment in Bohr magnetons,

$$\mu/\mu_B = -g/2 = -1.001\ 159\ 652\ 181\ 78\ (77) \quad [0.77\text{ ppt}], \tag{1.2}$$

though the uncertainty in this "calculated" value is mostly from the uncertainty with which the independent value of α is measured.

The more precisely measured electron moment, the improved standard model calculations, and the more precise independently measured value of α present the Standard Model with its most stringent test. The difference between the predicted magnetic moment $\mu(SM)$ and the measured electron magnetic moment μ is

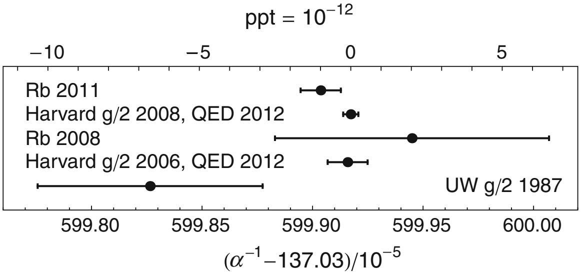

Fig. 1.2 The most accurate determinations of α are determined from the measured electron $g/2$ and standard model theory. The best independently measured value relies on measurements of a Rb atom recoil, the Rydberg constant, and several mass ratios

$$\frac{\mu-\mu(SM)}{\mu} = 0.000\,000\,000\,001\,05\ (82)\ [0.82\ \ \text{ppt}], \tag{1.3}$$

$$= 1.1\ (0.8)\times 10^{-12}\ [0.8\ \ \text{ppt}]. \tag{1.4}$$

The measurement and the prediction agree to 1.4 standard deviations (Fig. 1.1). The strikingly precise agreement to better than 12 significant figures is arguably the greatest triumph of the Standard Model and QED.

Fine Structure Constant

The electron magnetic moment is measured much more precisely than the fine structure constant. The result is that the fine structure constant is determined most precisely from the measurement of the electron moment and the Standard Model calculation (QED plus hadronic contributions) to be

$$\begin{aligned}\alpha^{-1} &= 137.035\,999\,173\,(33)\,(8)\ \ [0.24\ \text{ppb}]\,[0.06\ \text{ppb}],\\ &= 137.035\,999\,173\,(34)\qquad [0.25\ \text{ppb}],\end{aligned} \tag{1.5}$$

and is compared with all other precise measurements in Fig. 1.2. The total 0.25 ppb uncertainty is now mostly from the measurement (0.24 ppb) rather than from the Standard Model calculations (0.06 ppb). (Until last year the theoretical uncertainty was slightly larger than the experimental uncertainty.)

Antiproton Charge-to-Mass Ratio

The most precise test of the CPT theorem of the Standard Model made with a baryon and an antibaryon is a comparison of the charge-to-mass ratios of the antiproton and proton [8, 9],

$$\frac{\frac{q}{m}(\overline{\text{p}})}{\frac{q}{m}(p)} = -0.999\,999\,999\,839\ (90)\quad [90\ \text{ppt}]. \tag{1.6}$$

It is intriguing that this ratio is greater than the -1 predicted by the CPT theorem by 161 (90) ppt, which is about 1.8 standard deviations. Does this suggest that the

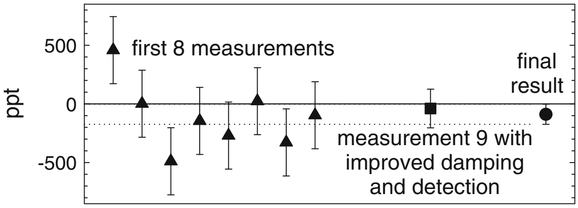

Fig. 1.3 Nine measurements of fractional differences in $|q/m|$ for the $\bar{p}$ and p, and their weighted average

magnitude of the charge-to-mass ratios of the antiproton and proton differ? It would be premature to make this conclusion insofar as the uncertainties were assigned to represent a standard deviation, and thus there is a reasonable probability that the true ratio could lie slightly outside the quoted uncertainty (Fig. 1.3).

A much more accurate measurement of q/m for the antiproton could certainly be carried out. This is most evident in the series of measurements that went into the final determination of q/m for the antiproton. An apparatus and technique improvement made the last 1-day measurement to be much more accurate than the earlier 8 measurements. Before this new level of accuracy could be exploited, unfortunately, LEAR closed down. Our ATRAP collaboration intends to make a more precise measurement.

Antiproton Magnetic Moment

The first one-particle measurement of the antiproton magnetic moment in nuclear magnetons,

$$\mu_{\bar{\mathrm{p}}}/\mu_N = -2.792\,845 \pm 0.000\,012 \quad [4.4\ \mathrm{ppm}]. \tag{1.7}$$

has just been reported [10]. Again the negative μ indicates that the magnetic moment $\boldsymbol{\mu}$ points opposite to the spin $\mathbf{S}$, with $\boldsymbol{\mu} = \mu\hat{\mathbf{S}}$ and $\hat{\mathbf{S}} = \mathbf{S}/(\hbar/2)$. The uncertainty is 680 times smaller than for any previous measurement (Fig. 1.4). To this precision, the measurement is consistent with the prediction of the Standard Model and its CPT theorem that the antiproton and proton have exactly opposite magnetic moments—equal in magnitude but opposite in sign.

This first precise antiproton magnetic moment measurement did not resolve individual spin flips for quantum jump spectroscopy as was done for the electron measurement. With a trapped proton, however, the possibility to resolve one-proton spin flips was reported even more recently by our Harvard group [11] and by a group from Mainz [12]. These demonstrations bode well for future increases in precision that could eventually improve by a factor as large as 10^4. A participant in this latter effort, S. Ulmer, discusses their proton measurements and their antiproton aspirations in a chapter in this volume.

Better Electron and Positron Magnetic Moment Measurements

An entirely new apparatus has been constructed at Harvard for making a much more precise comparison of the positron and electron magnetic moments, and for

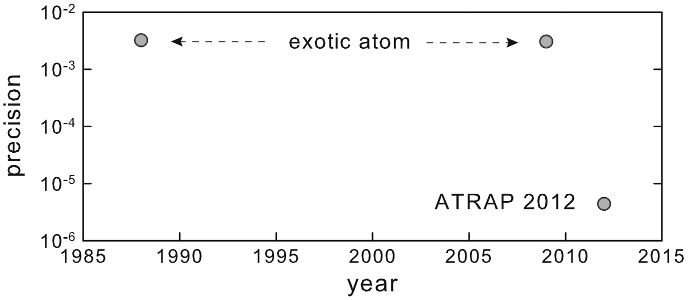

Fig. 1.4 Uncertainties in measurements of the $\overline{p}$ magnetic moment measured in nuclear magnetons. From [10]

more precise electron magnetic moment measurements. Positrons have recently been captured in this apparatus as preparation for measuring the positron magnetic moment at the electron precision. It should be possible to thereby make a lepton CPT test that compares positron and electron magnetic moments 15–20 times more precisely than a previous comparison [5]. The positron magnetic measurement will be followed with an attempt to measure the electron and positron magnetic moments at a much higher precision since no uncertainty that would prevent a substantial increase in precision has yet been identified.

Aspirations to Compare of Antihydrogen and Hydrogen

The possibility to use low energy antiprotons to make low energy antihydrogen cold enough to be trapped for precise measurements was proposed long ago [13] just after antiprotons were first captured in an ion trap [14]. The proposed goal was precise comparisons of antihydrogen and hydrogen, made at a precision that exceeds other precise tests of CPT invariance and the Standard Model with leptons and baryons. Now three collaborations are using cold antiprotons to produce cold antihydrogen to pursue this goal, and a fourth hopes to do so soon.

The nested Penning trap was invented to make possible the interaction of oppositely charged antiprotons and positrons that are trapped simultaneously during the positron cooling of the antiprotons. Essentially all the antihydrogen produced so far was produced using this device and method, by ATRAP [15, 16] and ATHENA [17] in 2002, and then by ASACUSA in 2010 [18].

ATRAP has also demonstrated a second method for producing antihydrogen, though much less antihydrogen has been produced so far. Lasers were used to control resonant charge exchange [19, 20]. ATRAP recently greatly increased the number of $\overline{\mathrm{H}}$ atoms produced by this second method, and plans to attempt to trap atoms so produced when CERN restarts antiproton production.

The proposal to trap cold antihydrogen in its ground state in a neutral particle trap [13] has so far been realized by ALPHA [21] and ATRAP [22]. However, the largest number of ground state $\overline{\mathrm{H}}$ atoms trapped per trial so far (Fig. 1.5) is ATRAP's 5 ± 1 atoms per trial [22]. More simultaneously trapped $\overline{\mathrm{H}}$ atoms are clearly needed, and no precise comparisons of antihydrogen and hydrogen have been made to date.

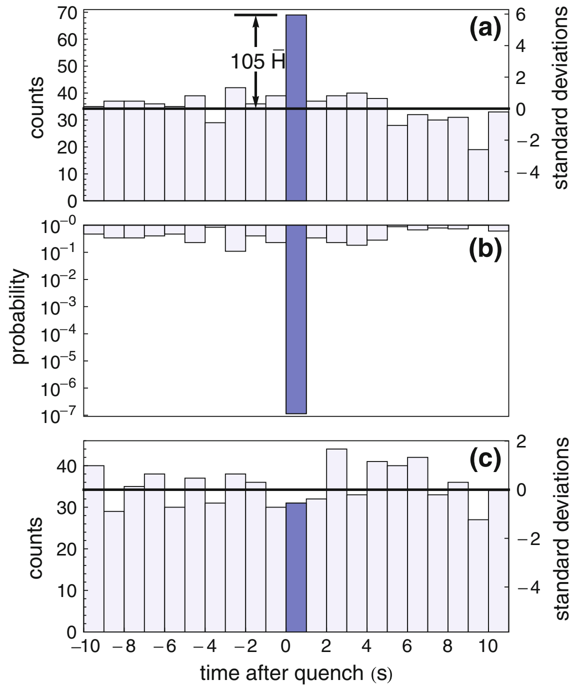

Fig. 1.5 The largest number of simultaneously trapped, ground state $\overline{\mathrm{H}}$ atoms is ATRAP's 5 $\pm$ 1 atoms per trial. (**a**) Detector counts in 1 s intervals for 20 trials. The radial Ioffe trap field turns off and releases trapped $\overline{\mathrm{H}}$ between $t = 0$ and 1 s. The counts in this interval above the average cosmic ray counts (*solid line*) correspond to 105 trapped $\overline{\mathrm{p}}$ for our detection efficiency. (**b**) Probability that cosmic rays produce the observed counts or more. (**c**) Quenching the Ioffe trap generates no false signals in 20 control trials

Antihydrogen experiments are mentioned here because of their promise for the future. It is hoped that precise comparisons of the antihydrogen and hydrogen will eventually reach a precision higher than the precise tests summarized above. J. Hangst of the ALPHA collaboration has provided a chapter in this volume on antihydrogen experiments.

1.2 Magnetic Moments

An electron with charge $-e$ with mass m in a magnetic field $B\hat{\mathbf{z}}$ circles in a cyclotron orbit with angular frequency $eB/m\hat{\mathbf{z}}$ and a magnetic moment

$$\boldsymbol{\mu} = -\frac{e}{2m}\mathbf{L} = -\mu_B \frac{\mathbf{L}}{\hbar}. \tag{1.8}$$

The Bohr magneton $\mu_B = e\hbar/(2m)$ gives the scale of the magnetic moment insofar as the orbital angular momentum $\mathbf{L}$ comes in units of $\hbar$ for a quantum system. The magnetic moment for an antiproton cyclotron orbit is instead scaled by the nuclear magneton, μ_N, which is about 2,000 times smaller than μ_B, by the ratio of the electron and proton masses.

The magnetic moment from the electron spin $\mathbf{S} = \frac{1}{2}\hbar\boldsymbol{\sigma}$ is often written in terms of the dimensionless Pauli operator $\boldsymbol{\sigma}$ for a spin 1/2 particle. It is also often written equivalently in terms of a dimensionless g value.

$$\boldsymbol{\mu} = \mu\boldsymbol{\sigma} = -g\frac{e}{2m}\mathbf{S} = -\frac{g}{2}\mu_B\boldsymbol{\sigma}. \tag{1.9}$$

The electron magnetic moment in Bohr magnetons is thus given by $\mu/\mu_B = -g/2$ which is the dimensionless size of the magnetic moment that must be measured and calculated. For an antiproton, the analogous dimensionless constant to be measured and calculated instead is the antiproton magnetic moment in nuclear magnetons, $\mu_{\bar{p}}/\mu_N \equiv -g_{\bar{p}}/2$.

The electron magnetic moment in Bohr magnetons can be very precisely calculated within the Standard Model of particle physics. It has the form

$$g/2 = 1 + a_{QED}(\alpha) + a_{hadronic} + a_{weak}. \tag{1.10}$$

The leading term $g/2 = 1$ is a prediction of the Standard Model insofar as it is the Dirac equation prediction for a point particle. Quantum electrodynamics (QED) gives the Standard Model prediction that vacuum fluctuations and polarization slightly increase $g/2$ by the small "anomaly" $a_{QED}(\alpha) \approx 10^{-3}$ that is a function of the fine structure constant α. The hadronic addition calculated within the Standard Model is much smaller, and the weak interaction addition is negligible at the current level of precision. One intriguing question is whether electron substructure (or other deviations from the Standard Model) could make $g/2$ deviate by the addition of some a_{new} from the Standard Model prediction to Eq. 1.10, as quark-gluon substructure does for an antiproton and proton.

Why measure the electron magnetic moment in Bohr magnetons, $g/2$? The motivations include:

1. The magnetic moment in Bohr magnetons is the property that can be most accurately measured for an electron—the important component of our universe that is unusual in that no internal structure has been predicted or detected.
2. The most stringent test of QED comes from measuring $g/2$ and comparing to the value $g(\alpha)$ calculated using an independently determined α in Eq. 1.10.
3. The most accurate determination of the fine structure constant comes from solving Eq. 1.10 for α in terms of the measured $g/2$. (No physics beyond the Standard Model, i.e. $a_{new} = 0$, is assumed.)
4. A search for physics beyond the Standard Model (e.g. electron substructure) comes from using the best measurement of $g/2$ and the best independent α (with

calculated values of $a_{hadronic}$ and a_{weak}) in Eq. 1.10 to set a limit on a possible a_{new} addition.
5. Comparing $g/2$ for an electron and a positron is the most stringent test of CPT invariance with leptons.

Owing to the great importance of the dimensionless magnetic moment, there have been many measurements of the electron $g/2$. A long list of measurements of this fundamental quantity has been compiled [4]. Worthy of special mention is a long series of measurements at the University of Michigan [23]. The spin precession relative to the cyclotron rotation of keV electrons was measured. Also worthy of special mention is the series of measurements at the University of Washington [5, 24].

Our measurements, like the UW measurements, made use of a single electron in a Penning trap. We were able to measure the electron magnetic moment about 15 times more precisely, and show that the measured value was different by about 1.7 standard deviations (Fig. 1.1).

The unifying idea for the new methods is that of a one-electron quantum cyclotron—with fully resolved cyclotron and spin energy levels, and a detection sensitivity sufficient to detect one quantum transitions is achieved in our fully quantum measurements [1, 2].

The substantially higher accuracy of the new measurements was the result of new experimental methods, developed and demonstrated one thesis at a time over 20 years by a string of excellent Ph.D. students—C.H. Tseng, D. Enzer, J. Tan, S. Peil, B. D'Urso, B. Odom and D. Hanneke. The new methods included:

1. A cylindrical Penning trap was used to suspend the electron. The cylindrical trap was invented to form a microwave cavity that could inhibit spontaneous emission. The calculable cavity shape made it possible to understand and correct for cavity shifts of the measured cyclotron frequency.
2. Cavity-inhibited spontaneous emission (by a factor of up to 250) narrowed measured linewidths and gave us the crucial averaging time that we needed to resolve one-quantum changes in the electron's cyclotron state.
3. The cavity was cooled to 100 mK rather than to 4.2 K so that in thermal equilibrium the electron's cyclotron motion would be in its ground state.
4. Detection with good signal-to-noise ratio came from feeding back a signal derived from the electron's motion along the magnetic field to the electron to cancel the damping due to the detection impedance. The "classical measurement system" for the quantum cyclotron motion was this large self-excited motion of the electron, with a quantum nondemolition coupling between the classical and quantum systems.
5. A silver trap cavity avoided the magnetic field variations due to temperature fluctuations of the paramagnetism of conventional copper trap electrodes.
6. The measurement was entirely automated so that the best data could be taken at night, when the electrical, magnetic and mechanical disturbances were lowest, with no person present.
7. A parametric excitation of electrons suspended in the trap was used to measure the radiation modes of the radiation field in the trap cavity.

8. The damping rate of a single trapped electron was used as a second probe of the radiation fields within the trap cavity.

1.3 One-Electron Quantum Cyclotron

1.3.1 A Homemade Atom

A one-electron quantum cyclotron is a single electron suspended within a magnetic field, with the quantum structure in its cyclotron motion fully resolved. Accurate measurements of the resonant frequencies of driven transitions between the energy levels of this homemade atom—an electron bound to our trap—reveals the electron magnetic moment in units of Bohr magnetons, $g/2$. The energy levels and what must be measured to determine $g/2$ are presented in this section. The experimental devices and methods needed to realize the one-electron quantum cyclotron are discussed in following sections.

A nonrelativistic electron in a magnetic field has energy levels

$$E(n, m_s) = \frac{g}{2} h\nu_c m_s + (n + \tfrac{1}{2}) h\nu_c. \tag{1.11}$$

These depend in a familiar way upon the electron's cyclotron frequency ν_c and its spin frequency $\nu_s \equiv (g/2)\nu_c$. The electron $g/2$ is thus specified by the two frequencies,

$$\frac{g}{2} = \frac{\nu_s}{\nu_c} = 1 + \frac{\nu_s - \nu_c}{\nu_c} = 1 + \frac{\nu_a}{\nu_c}, \tag{1.12}$$

or equivalently by their difference (the anomaly frequency $\nu_a \equiv \nu_s - \nu_c$) and ν_c. Because ν_s and ν_c differ by only a part-per-thousand, measuring ν_a and ν_c to a precision of 1 part in 10^{10} gives $g/2$ to 1 part in 10^{13}.

Although one electron suspended in a magnetic field will not remain in one place long enough for a measurement, two features of determining $g/2$ by measuring ν_a and ν_c are apparent in Eq. 1.12.

1. Nothing in physics can be measured more accurately than a frequency (the art of time keeping being so highly developed) except for a ratio of frequencies.
2. Although both of these frequencies depend upon the magnetic field, the field dependence drops out of the ratio. The magnetic field thus needs to be stable only on the time scale on which both frequencies can be measured, and no absolute calibration of the magnetic field is required.

To confine the electron for precise measurements, an ideal Penning trap includes an electrostatic quadrupole potential $V \sim z^2 - \frac{1}{2}\rho^2$ with a magnetic field $B\hat{\mathbf{z}}$ [25]. This potential shifts the cyclotron frequency from the free-space value ν_c to $\bar{\nu}_c$. The latter frequency is also slightly shifted by the unavoidable leading imperfections of a real

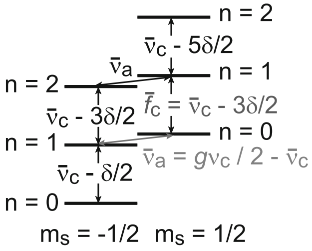

Fig. 1.6 Lowest cyclotron and spin levels of an electron in a Penning trap

laboratory trap—a misalignment of the symmetry axis of the electrostatic quadrupole and the magnetic field, and quadratic distortions of the electrostatic potential.

The lowest cyclotron energy levels (with quantum numbers $n = 0, 1, \ldots$) and the spin energy levels (with quantum numbers $m_s = \pm 1/2$) are given by

$$E(n, m_s) = \tfrac{g}{2} h\nu_c m_s + (n + \tfrac{1}{2})h\bar{\nu}_c - \tfrac{1}{2}h\delta(n + \tfrac{1}{2} + m_s)^2. \tag{1.13}$$

The lowest cyclotron and spin energy levels are represented in Fig. 1.6.

Special relativity is important for even the lowest quantum levels. The third term in Eq. 1.13 is the leading relativistic correction [25] to the energy levels. Special relativity makes the transition frequency between two cyclotron levels $|n, m_s\rangle \leftrightarrow |n+1, m_s\rangle$ decrease from $\bar{\nu}_c$ to $\bar{\nu}_c + \varDelta\bar{\nu}_c$, with the shift

$$\varDelta\bar{\nu}_c = -\delta(n + 1 + m_s) \tag{1.14}$$

depending upon the spin state and cyclotron state. This very small shift, with

$$\delta/\nu_c \equiv h\nu_c/(mc^2) \approx 10^{-9}, \tag{1.15}$$

is nonetheless significant at our precision. An important new feature of our measurement is that special relativity adds no uncertainty to our measurements. Quantum transitions between identified energy levels with a precisely known relativistic contribution to the energy levels are resolved. When the average cyclotron frequency of an unknown distribution of cyclotron states was all that could be measured [5], figuring out the size of the relativistic frequency shift was difficult.

We have seen how $g/2$ is determined by the anomaly frequency ν_a and the free-space cyclotron frequency $\nu_c = eB/(2\pi m)$. However, neither of these frequencies is an eigenfrequency of the trapped electron. We actually measure the transition frequencies

$$\bar{f}_c \equiv \bar{\nu}_c - \frac{3}{2}\delta \tag{1.16}$$

$$\bar{\nu}_a \equiv \frac{g}{2}\nu_c - \bar{\nu}_c \tag{1.17}$$

represented by the arrows in Fig. 1.6 for an electron initially prepared in the state $|n = 0, m_s = 1/2\rangle$.

The needed $\nu_c = eB/(2\pi m)$ is deduced from the three observable eigenfrequencies of an electron bound in the trap by the Brown-Gabrielse invariance theorem [26],

$$(\nu_c)^2 = (\bar{\nu}_c)^2 + (\bar{\nu}_z)^2 + (\bar{\nu}_m)^2. \tag{1.18}$$

The three measurable eigenfrequencies on the right include the cyclotron frequency $\bar{\nu}_c$ for the quantum cyclotron motion we have been discussing. The second measurable eigenfrequency is the axial oscillation frequency $\bar{\nu}_z$ for the nearly-harmonic, classical electron motion along the direction of the magnetic field. The third measurable eigenfrequency is the magnetron oscillation frequency for the classical magnetron motion along the circular orbit for which the electric field of the trap and the motional electric field exactly cancel.

The invariance theorem applies for a perfect Penning trap, but also in the presence of the mentioned imperfection shifts of the eigenfrequencies for an electron in a trap. This theorem, together with the well-defined hierarchy of trap eigenfrequencies, $\bar{\nu}_c \gg \bar{\nu}_z \gg \bar{\nu}_m \gg \delta$, yields an approximate expression that is sufficient at our accuracy. We thus determine the electron $g/2$ using

$$\frac{g}{2} = \frac{\bar{\nu}_c + \bar{\nu}_a}{\nu_c} \simeq 1 + \frac{\bar{\nu}_a - \bar{\nu}_z^2/(2\bar{f}_c)}{\bar{f}_c + 3\delta/2 + \bar{\nu}_z^2/(2\bar{f}_c)} + \frac{\Delta g_{cav}}{2}. \tag{1.19}$$

The cavity shift $\Delta g_{cav}/2$ that arises from the interaction of the cyclotron motion and the trap cavity is presently discussed in detail.

1.3.2 Cylindrical Penning Trap Cavity

A cylindrical Penning trap (Fig. 1.7) is the key device that makes these measurements possible. It was invented [27] and demonstrated [28] to provide boundary conditions that produce a controllable and understandable radiation field within the trap cavity, along with the needed electrostatic quadrupole potential. Spontaneous emission can be significantly inhibited at the same time as corresponding shifts of the electron's oscillation frequencies are avoided. We shall see that this is critical to the new Harvard measurements in several ways (Table 1.1).

A necessary function of the trap electrodes is to produce a very good approximation to an electrostatic quadrupole potential. This is possible with cylindrical electrodes but only if the relative geometry of the electrodes is carefully chosen [27]. The electrodes of the cylindrical trap are symmetric under rotations about the center axis ($\hat{\mathbf{z}}$), which is parallel to the spatially uniform magnetic field ($B\hat{\mathbf{z}}$). The potential (about 100 V) applied between the endcap electrodes and the ring electrode provides the basic trapping potential and sets the axial frequency $\bar{\nu}_z$ of the nearly harmonic oscillation of the electron parallel to the magnetic field. The potential applied to the

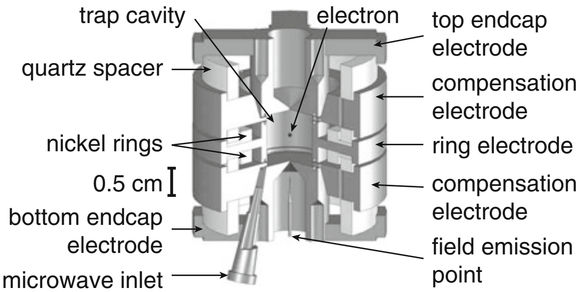

Fig. 1.7 Cylindrical Penning trap cavity used to confine a single electron and inhibit spontaneous emission

Table 1.1 Properties of the trapped electron

Cyclotron frequency	$\omega_c/(2\pi)$	150 GHz
Trap-modified cyc. freq.	$\omega_+/(2\pi)$	150 GHz
Axial frequency	$\omega_z/(2\pi)$	200 MHz
Magnetron frequency	$\omega_-/(2\pi)$	133 kHz
Cyclotron damping (free space)	τ_+	0.09 s
Axial damping	τ_z	200 ms
Magnetron damping	τ_-	10^9 yr

compensation electrodes is adjusted to tune the shape of the potential, to make the oscillation as harmonic as possible. The tuning does not change $\bar{\nu}_z$ very much owing to an orthogonalization [27, 29] that arises from the geometry choice. What we found was that one electron could be observed within a cylindrical Penning trap with as good or better signal-to-noise ratio than was realized in hyperbolic Penning traps.

The principle motivation for the cylindrical Penning trap is to form a microwave cavity whose radiation properties are well understood and controlled—the best possible approximation to a perfect cylindrical trap cavity. (Our calculation attempts with a hyperbolic trap cavity were much less successful [30].) The modes of the electromagnetic radiation field that are consistent with this boundary condition are the well known transverse electric TE$_{mnp}$ and transverse magnetic TE$_{mnp}$ modes (see e.g. [31, Sect. 8.7]).

For a right circular cylinder of diameter $2\rho_0$ and height $2z_0$ the TE and TM modes have characteristic resonance frequencies,

$$TE: \quad \omega_{mnp} = c\sqrt{\left(\frac{x'_{mn}}{\rho_0}\right)^2 + \left(\frac{p\pi}{2z_0}\right)^2} \tag{1.20a}$$

$$TM: \quad \omega_{mnp} = c\sqrt{\left(\frac{x_{mn}}{\rho_0}\right)^2 + \left(\frac{p\pi}{2z_0}\right)^2}. \tag{1.20b}$$

They are indexed with integers

$$m = 0, 1, 2, \ldots \tag{1.21}$$

$$n = 1, 2, 3, \ldots \tag{1.22}$$

$$p = 1, 2, 3, \ldots, \tag{1.23}$$

and are functions of the nth zeros of Bessel functions and their derivatives

$$J_m(x_{mn}) = 0 \tag{1.24}$$

$$J'_m(x'_{mn}) = 0 \tag{1.25}$$

The zeros force the boundary conditions at the cylindrical wall. All but the $m = 0$ modes are doubly degenerate.

Of primary interest is the magnitude of the cavity electric fields that couple to the cyclotron motion of an electron suspended in the center of the trap. For both TE and TM modes, the transverse components of **E** are proportional to

$$\sin(\tfrac{p\pi}{2}(\tfrac{z}{z_0} + 1)) = \begin{cases} (-1)^{p/2} \sin(\frac{p\pi z}{2z_0}) & \text{for even } p, \\ (-1)^{(p-1)/2} \cos(\frac{p\pi z}{2z_0}) & \text{for odd } p. \end{cases} \tag{1.26}$$

For an electron close to the cavity center, ($z \approx 0$), only modes with odd p thus have any appreciable coupling.

The transverse components of the electric fields are also proportional to either the order-m Bessel function times m/ρ for the TE modes, or to the derivative of the order-m Bessel function for the TM modes. Close to the cavity center ($\rho \approx 0$),

$$\frac{m}{\rho}\, J_m(x^{(\prime)}_{mn}\tfrac{\rho}{\rho_0}) \sim \begin{cases} \dfrac{\rho^{m-1}}{(m-1)!}\left(\dfrac{x^{(\prime)}_{mn}}{2\rho_0}\right)^m & \text{for } m > 0 \\ 0 & \text{for } m = 0 \end{cases} \tag{1.27a}$$

$$\frac{x^{(\prime)}_{mn}}{\rho_0} J'_m(x^{(\prime)}_{mn}\tfrac{\rho}{\rho_0}) \sim \begin{cases} \dfrac{\rho^{m-1}}{(m-1)!}\left(\dfrac{x^{(\prime)}_{mn}}{2\rho_0}\right)^m & \text{for } m > 0 \\ -\dfrac{x^{(\prime)2}_{0n}}{2\rho_0^2}\rho & \text{for } m = 0. \end{cases} \tag{1.27b}$$

In the limit $\rho \to 0$, all but the $m = 1$ modes vanish.

For a perfect cylindrical cavity the only radiation modes that couple to an electron perfectly centered in the cavity are $\mathrm{TE}_{1n(\mathrm{odd})}$ and $\mathrm{TE}_{1n(\mathrm{odd})}$. If the electron is moved slightly off center axially it will begin to couple to radiation modes with $mnp = 1n(\text{even})$. If the electron is moved slightly off-center radially it similarly begins to couple to modes with $m \neq 1$.

In the real trap cavity, the perturbation caused by the small space between the electrodes is minimized by the use of “choke flanges”—small channels that tend to reflect the radiation leaking out of the trap back to cancel itself, and thus to minimize the losses from the trap. The measured radiation modes, discussed later, are close enough to the calculated frequencies for a perfect cylindrical cavity that we have been able to identify more than 100 different radiation modes for such trap cavities [32–34]. The spatial properties of the electric and magnetic field for the radiation that builds up within the cavity are thus quite well understood. Some of the modes couple to cyclotron motion of an electron centered in the cavity, others couple to the spin of a centered electron, and still others have the symmetry that we hope will one day allow us to sideband-cool the axial motion.

1.3.3 100 mK *and 5 T*

Detecting transitions between energy levels of the quantum cyclotron requires that the electron-bound-to-the-trap system be prepared in a definite quantum state. Two key elements are a high magnetic field, and a low temperature for the trap cavity. A high field makes the spacing of the cyclotron energy levels to be large. A high field and low temperature make a very large Boltzmann probability to be in the lowest cyclotron state, $P \propto \exp[-h\bar{\nu}_c/(kT)]$, which is negligibly different from unity.

The trap cavity is cooled to 0.1 K or below via a thermal contact with the mixing chamber of an Oxford Instruments Kelvinox 300 dilution refrigerator (Fig. 1.8). The electrodes of this trap cavity are housed within a separate vacuum enclosure that is entirely at the base temperature. Measurements on an apparatus with a similar design but at 4.2 K found the vacuum in the enclosure to be better than 5×10^{-17} torr [35]. Our much lower temperature make our background gas pressure much lower. We are able to keep one electron suspended in our apparatus for as long as desired—regularly months at a time. Substantial reservoirs for liquid helium and liquid nitrogen make it possible to keep the trap cold for five to seven days before the disruption of adding more liquid helium or nitrogen is required.

The trap and its vacuum container are located within a superconducting solenoid (Fig. 1.8) that makes a very homogeneous magnetic field over the interior volume of the trap cavity. A large dewar sitting on top of the solenoid dewar provides the helium needed around the dilution refrigerator below. The superconducting solenoid is entirely self-contained, with a bore that can operate from room temperature down to 77 K. It possesses shim coils capable of creating a field homogeneity better than a part in 10^8 over a 1 cm diameter sphere and has a passive “shield” coil that reduces fluctuations in the ambient magnetic field [36, 37]. When properly energized (and after the steps described in the next section have been taken) it achieves field stability better than a part in 10^9 per hour. We regularly observe drifts below 10^{-9} per night.

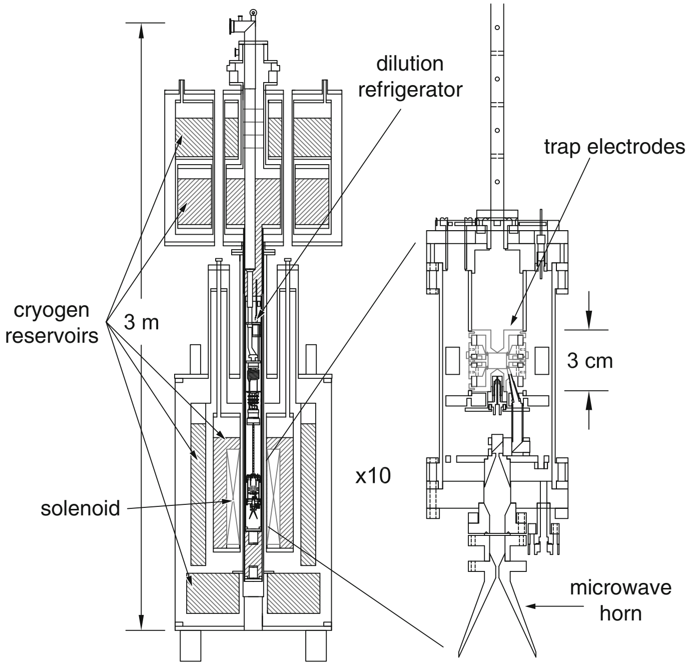

Fig. 1.8 The apparatus includes a trap electrodes near the central axis, surrounded by a superconducting solenoid. The trap is suspended from a dilution refrigerator

1.3.4 Stabilizing the Energy Levels

Measuring the electron $g/2$ with a precision of parts in 10^{13} requires that the energy levels of our homemade atom, an electron bound to a Penning trap, be exceptionally stable. The energy levels depend upon the magnetic field and upon the the potential that we apply to the trap electrodes. The magnetic field must be stable at least on the time scale that is required to measure the two frequencies, $\bar{f}_c$ and $\bar{\nu}_a$, that are both proportional to the magnetic field.

One defense against external field fluctuations is a high magnetic field. This makes it so that field fluctuations due to outside sources are relatively smaller. The largest source of ambient magnetic noise is a subway that produces 50 nT (0.5 mG, 10 ppb) fluctuations in our lab and that would limit us to four hours of data taking per day (when the subway stops running) if we did not shield the electron from them. Eddy currents in the high-conductivity aluminum and copper cylinders of the dewars and the magnet bore shield high-frequency fluctuations [38]. For slower fluctuations, the aforementioned self-shielding solenoid [36] has the correct geometry to make the central field always equal to the average field over the solenoid cross-section. This translates flux conservation into central-field conservation, shielding external fluctuations by more than a factor of 150 [37].

Stabilizing the field produced by the solenoid requires that care is taken when the field value is changed, since changing the current in the solenoid alters the forces between windings. Resulting stresses can take months to stabilize if the coil is not pre-stressed by “over-currenting” the magnet. Our recipe is to overshoot the target value by a few percent of the change, undershoot by a similar amount, and then move to the desired field.

The apparatus in Fig. 1.8 evolved historically rather than being designed for maximum magnetic field stability in the final configuration. Because the solenoid and the trap electrodes are suspended from widely separated support points, temperature and pressure changes can cause the electrodes to move relative to the solenoid. Apparatus vibrations can do the same insofar as the magnetic field is not perfectly homogeneous, despite careful adjusting of the persistent currents in ten superconducting shim coils. Any relative motion of the electron and solenoid changes the field seen by the electron.

To counteract this, we regulate the five He and N_2 pressures in the cryostats to maintain the temperature of both the bath and the solenoid itself [39, 40]. Recently we also relocated the dilution refrigerator vacuum pumps to an isolated room at the end of a 12 m pipe run. This reduced vibration by more than an order of magnitude at frequencies related to the pump motion and reduced the noise level for the experimenters but did not obviously improve the $g/2$ data.

Because some of the structure establishing the relative location of the trap electrodes and the solenoid is at room temperature, changes in room temperature can move the electron in the magnetic field. The lab temperature routinely cycles 1–2 K daily, so we house the apparatus in a large, insulated enclosure within which we actively regulate the air temperature to 0.1 K. A refrigerated circulating bath (ThermoNeslab RTE-17) pumps water into the regulated zone and through an automobile transmission fluid radiator, heating and cooling the water to maintain constant air temperature. Fans couple the water and air temperatures and keep a uniform air temperature throughout.

The choice of materials for the trap electrodes and its vacuum container is also crucial to attaining high field stability [1, 41]. Copper trap electrodes, for example, have a nuclear paramagnetism at 100 mK that makes the electron see a magnetic field that changes at an unacceptable level with very small changes in trap temperature. We thus use only low-Curie-constant materials such as silver, quartz, titanium, and molybdenum at the refrigerator base temperature and we regulate the mixing chamber temperature to 1 mK or better.

A stable axial frequency is also extremely important since small changes in the measured axial frequency reveal one-quantum transitions of the cyclotron and spin energy (as will be discussed in Sect. 1.4.1). A trapping potential without thermal fluctuations is provided by a charged capacitor (10 μF) that has a very low leakage resistance at low temperature. We add to or subtract from the charge on the capacitor using 50 ms current pulses sent to the capacitor through a 100 MΩ resistor as needed to keep the measured axial frequency constant. Because of the orthogonalized trap design [27] already discussed, the potential applied to the compensation electrodes (to make the electron see as close to a pure electrostatic quadrupole potential as possible) has little effect upon the axial frequency.

1.3.5 Motions and Damping of the Suspended Electron

We load a single electron using an electron beam from a sharp tungsten field emission tip. A hole in the bottom endcap electrode admits the beam, which hits the top endcap electrode and releases gas atoms cryopumped on the surface. Collisions between the beam and gas atoms eventually cause an electron to fall into the trap. Adjusting the beam energy and the time it is on determines the number of electrons loaded.

The electron has three motions in the Penning trap formed by the $B = 5.4$ T magnetic field, and the electrostatic quadrupole potential. The cyclotron motion in the trap has a cyclotron frequency $\bar{\nu}_c \approx 150\,\text{GHz}$. The axial frequency, for the harmonic oscillator parallel to the magnetic field direction, is $\bar{\nu}_z \approx 200\,\text{MHz}$. A circular magnetron motion, perpendicular to **B**, has an oscillation frequency, $\bar{\nu}_m \approx 133\,\text{kHz}$. The spin precession frequency, which we do not measure directly, is slightly higher than the cyclotron frequency. The frequency difference is the anomaly frequency, $\bar{\nu}_a \approx 174\,\text{MHz}$, which we do measure directly.

The undamped spin motion is essentially uncoupled from its environment [25]. The cyclotron motion is only weakly damped. By controlling the cyclotron frequency relative to that of the cavity radiation modes, we alter the density of radiation states and inhibit the spontaneous emission of synchrotron radiation [25, 42] by 10–50 times the $(90\,\text{ms})^{-1}$ free-space rate. Blackbody photons that could excite from the cyclotron ground state are eliminated because the trap cavity is cooled by the dilution refrigerator to 100 mK [43]. The axial motion is cooled by a resonant circuit at a rate $\gamma_z \approx (0.2\ \text{s})^{-1}$ to as low as 230 mK (from 5 K) when the detection amplifier is off. The magnetron radius is minimized with axial sideband cooling [25].

1.4 Non-destructive Detection of One-Quantum Transitions

1.4.1 QND Detection

Quantum nondemolition (QND) detection has the property that repeated measurements of the energy eigenstate of the quantum system do not change the state of the quantum system [44, 45]. This is crucial for detecting one-quantum transitions in the cyclotron motion insofar as it avoids transitions produced by the detection system. In this section we discuss the QND coupling, and in the next section the self-excited oscillator readout system.

Detecting a single 150 GHz photon from the decay of one cyclotron energy level to the level below would be very difficult—because the frequency is so high and because it is difficult to cover the solid angle into which the photon could be emitted. Instead we get the one-quantum sensitivity by coupling the cyclotron motion to the orthogonal axial motion at 200 MHz, a frequency at which we are able to make sensitive detection electronics [46]. The QND detection keeps the thermally driven axial motion of the electron from changing the state of the cyclotron motion.

We use a magnetic bottle gradient that is familiar from plasma physics and from earlier electron measurements [5, 47],

$$\boldsymbol{\Delta B} = B_2\left[\left(z^2 - \rho^2/2\right)\hat{\mathbf{z}} - z\rho\hat{\boldsymbol{\rho}}\right] \tag{1.28}$$

with $B_2 = 1540\,\mathrm{T/m^2}$. This is the lowest order gradient that is symmetric under reflections $z \to -z$ and is cylindrically symmetric about $\hat{\mathbf{z}}$. The gradient arises from a pair of thin nickel rings (Fig. 1.7) that are completely saturated in the strong field from the superconducting solenoid. To lowest order the rings modify B by $\approx -0.7\,\%$—merely changing the magnetic field that the electron experiences without affecting our measurement.

The formal requirement for a QND measurement is that the Hamiltonian of the quantum system (i.e. the cyclotron Hamiltonian) and the Hamiltonian describing the interaction of the quantum system and the classical measurement system must commute. The Hamiltonian that couples the quantum cyclotron and spin motions to the axial motion does so. It has the form $-\mu B$, where μ is the magnetic moment associated with the cyclotron motion or the spin. The coupling Hamiltonian thus has a term that goes as μz^2. This term has the same spatial symmetry as does the axial Hamiltonian, $H = \frac{1}{2}m(2\pi\bar{\nu}_z)^2 z^2$. A change in the magnetic moment that takes place from a one-quantum change in the cyclotron or spin magnetic moment thus changes the observed axial frequency of the suspended electron.

The result is that the frequency of the axial motion $\bar{\nu}_z$ shifts by

$$\Delta\bar{\nu}_z = \delta_B(n + m_s), \tag{1.29}$$

in proportion to the cyclotron quantum number n and the spin quantum number m_s. Figure 1.9 shows the $\Delta\bar{\nu}_z = 4\,\mathrm{Hz}$ shift in the 200 MHz axial frequency that takes

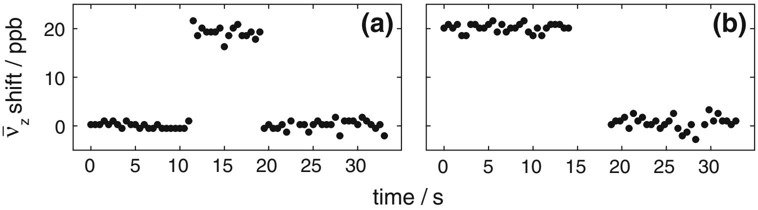

Fig. 1.9 Two quantum jumps: A cyclotron jump (**a**) and spin flip (**b**) measured via a QND coupling to shifts in the axial frequency

place for one-quantum changes in cyclotron (Fig. 1.9a) and spin energy (Fig. 1.9b). The 20 ppb shift is easy to observe with an averaging time of only 0.5 s. We typically measure with an averaging time that is half this value.

1.4.2 One-Electron Self-Excited Oscillator

The QND coupling makes small changes in the electron's axial oscillation frequency, the signature of one-quantum cyclotron transitions and spin flips. Measuring these small frequency changes is facilitated by a large axial oscillation amplitude. To this end we use electrical feedback which we demonstrated could be used effectively to either cool the axial motion [48] or to make a large self-excited axial oscillation [49]. Cyclotron excitations and spin flips are generally induced while the detection system is off, as will be discussed. After an attempt to excite the cyclotron motion or to flip the spin has been made, the detection system is then turned on. The self-excited oscillator rapidly reaches steady state, and its oscillation frequency is then measured by fourier transforming the signal.

The 200 MHz axial frequency lies in the radio-frequency (rf) range which is more experimentally accessible than the microwave range of the 150 GHz cyclotron and spin frequencies, as mentioned. Nevertheless, standard rf techniques must be carefully tailored for our low-noise, cryogenic experiment. The electron axial oscillation induces image currents in the trap electrodes that are proportional to the axial velocity of the electron [25, 50]. An inductor (actually the inductance of a cryogenic feedthrough) is placed in parallel with the capacitance between two trap electrodes to cancel the reactance of the capacitor which would otherwise short out the induced signal. The rf loss in the tuned circuit that is formed is an effective resistance that damps the axial motion.

The voltage that the electron motion induces across this effective resistance is amplified with two cryogenic detection amplifiers. The heart of each amplifier is a single-gate high electron mobility transistor (Fujitsu FHX13LG).

The first amplifier is at the 100 mK dilution refrigerator base temperature. Operating this amplifier without crashing the dilution refrigerator requires operating with a power dissipation in the FET that is three orders of magnitude below the transistor's 10 mW design dissipation. The effective axial temperature for the electron while current is flowing through the FET is about 5 K, well above the ambient temperature. Very careful heat sinking makes it possible for the effective axial temperature of the electron to cool to below 230 mK in several seconds after the amplifier is turned off, taking the electron axial motion to this temperature. Cyclotron excitations and spin flips are induced only when the axial motion is so cooled, with the detection amplifiers off, since the electron is then making the smallest possible excursion in the magnetic bottle gradient.

The second cryogenic amplifier is mounted on the nominally 600 mK still of the dilution refrigerator. This amplifier counteracts the attenuation of a thermally-isolating but lossy stainless steel transmission line that carries the amplified signal out of the refrigerator. The second amplifier boosts the signal above the noise floor of the first room-temperature amplifier.

Because the induced image-current signal is proportional to the electron's axial velocity, feeding this signal back to drive the electron alters the axial damping force, a force that is also proportional to the electron velocity. Changing the feedback gain thus changes the damping rate. As the gain increases, the damping rate decreases as does the effective axial temperature of the electron, in accord with the fluctuation dissipation theorem [51]. Feedback cooling of the one-electron oscillator from 5.2 to 850 mK was demonstrated [48]. The invariant ratio of the separately measured damping rate and the effective temperature was also demonstrated, showing that the amplifier adds very little noise to the feedback.

Setting the feedback gain to make the feedback drive exactly cancel the damping in the attached circuit could sustain a large axial oscillation amplitude, in principle. However, since the gain cannot be perfectly adjusted, noise fluctuations will always drive the axial oscillation exponentially away from equilibrium. We thus stabilize the oscillation amplitude using a digital signal processor (DSP) that Fourier transforms the signal in real time, and adjusts the feedback gain to keep the signal size at a fixed value.

The one-particle self-excited oscillator is turned on after an attempt has been made to excite the cyclotron energy up one level, or to flip the spin. The frequency of the axial oscillation that rapidly stabilizes at a large and easily detected amplitude is then measured. Small shifts in this frequency reveal whether the cyclotron motion has been excited by one quantum or whether the spin has flipped, as illustrated in Fig. 1.9.

1.4.3 Inhibited Spontaneous Emission

The spontaneous emission of synchrotron radiation in free space would make the damping time for an electron's cyclotron motion to be less than 0.1 s. This is not enough time to average down the noise in our detection system to the level that would allow the resolution of one-quantum transitions between cyclotron states. Also, to drive cyclotron transitions "in the dark", with the detection system off, requires that the cyclotron excitations persist long enough for the detection electronics to be turned on. Cavity-inhibition of the spontaneous emission gives us the averaging time that we need.

One of the early papers in what has come to be know as cavity QED was an observation of inhibited spontaneous emission within a Penning trap [42]—the first time that inhibited spontaneous emission was observed within a cavity and with only one particle—as anticipated earlier [52, 53]. As already mentioned, the cylindrical Penning trap [27] was invented to provide understandable boundary conditions to control the spontaneous emission rate with only predictable cavity shifts of the electron's cyclotron frequency.

The spontaneous emission rate is measured directly, by making a histogram of the time the electron spends in the first excited state after being excited by a microwave

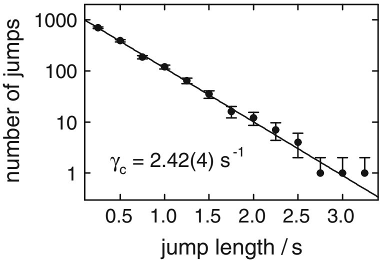

Fig. 1.10 A histogram of the time that the electron spends in the first excited state that is fit to an exponential reveals the substantial inhibition of the spontaneous emission of synchrotron radiation. The decay time, 0.41 s in this example, depends on how close the cyclotron frequency is to neighboring radiation modes of the trap cavity. Lifetimes as long as 16 s have been observed

drive injected into the trap cavity with the detector left on. Figure 1.10 shows a sample histogram which fits well to an exponential (solid curve) with a lifetime of 0.41 s in this example.

Stimulated emission is avoided by making these observations only when the cavity is at low temperature so that effectively no blackbody photons are present. The detector causes thermal fluctuations of the axial oscillation amplitude, and these in turn make the cyclotron frequency fluctuate. For measuring the cyclotron decay time, however, this does not matter as long as the fluctuations in axial amplitude are small compared to the 2 mm wavelength of the radiation that excites the cyclotron motion.

The spontaneous emission rate into free space is [25]

$$\gamma_+ = \frac{4}{3}\frac{r_e}{c}(\omega_c)^2 \approx \frac{1}{0.89\ \mathrm{ms}}\,. \tag{1.30}$$

The measured rate in this example is thus suppressed by a factor of 4.5. The density of states within the cylindrical trap cavity is not that of free space. Instead the density of states for the radiation is peaked at the resonance frequencies of the radiation modes of the cavity, and falls to very low values between the radiation modes. We attain the inhibited spontaneous emission by tuning the magnetic field so that the cyclotron frequency is as far as possible from resonance with the cavity radiation modes. With the right choice of magnetic field we have increased the lifetime to 16 s, which is a cavity suppression of spontaneous emission by a factor of 180.

In a following section we report on using the direct measurements of the radiation rate for electron cyclotron motion to probe the radiation modes of the cavity, with the radiation rate increasing sharply at frequencies that approach a resonant mode of the cavity.

1.5 Elements of a Electron $g/2$ Measurement

1.5.1 Quantum Jump Spectroscopy

We determine the cyclotron and anomaly frequencies using quantum jump spectroscopy, in which a near resonance drive attempts to either excite the cyclotron motion or flip the spin. After each attempt we check whether a one-quantum transition has taken place, and build up a histogram of transitions per attempt. Figure 1.11 shows the observed quantum jump lineshapes upon which our 2008 measurement is based.

A typical data run consists of alternating scans of the cyclotron and anomaly lines. The runs occur at night, with daytime runs only possible on Sundays and holidays when the ambient magnetic field noise is lower. Interleaved every three hours among these scans are periods of magnetic field monitoring to track long-term drifts using

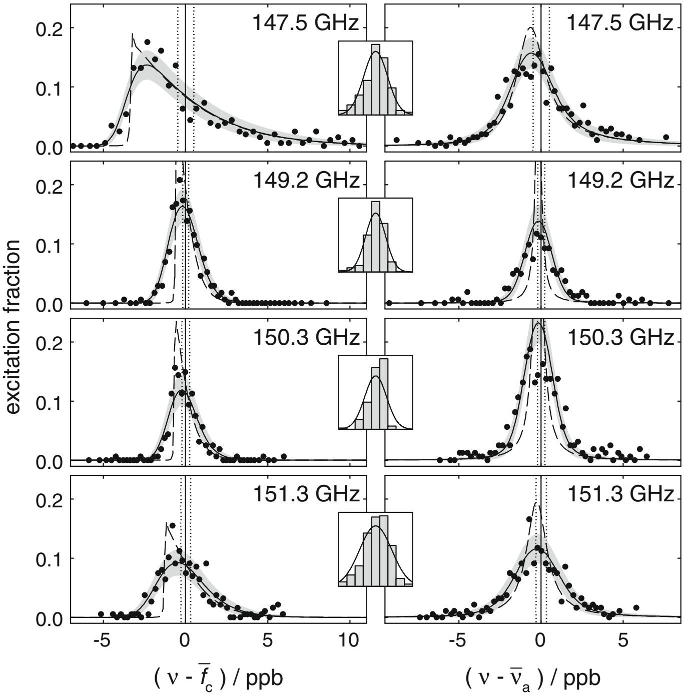

Fig. 1.11 Quantum-jump spectroscopy lineshapes for cyclotron (*left*) and anomaly (*right*) transitions with maximum-likelihood fits to broadened lineshape models (*solid*) and inset resolution functions (*solid*) and edge-tracking data (histogram). *Vertical lines* show the $1-\sigma$ uncertainties for extracted resonance frequencies. Corresponding unbroadened lineshapes are dashed. Gray bands indicate $1-\sigma$ confidence limits for distributions about broadened fits. All plots share the same relative frequency scale

the electron itself as the magnetometer. In addition, we continuously monitor over fifty environmental parameters such as refrigerator temperatures, cryogen pressures and flows, and the ambient magnetic field in the lab so that we may screen data for abnormal conditions and troubleshoot problems.

Cyclotron transitions are driven by injecting microwaves into the trap cavity. The microwaves originate as a 15 GHz drive from a signal generator (Agilent E8251A) whose low-phase-noise, 10 MHz oven-controlled crystal oscillator serves as the timebase for all frequencies in the experiment. After passing through a waveguide that removes all subharmonics, the signal enters a microwave circuit that includes an impact ionization avalanche transit-time (IMPATT) diode, which multiplies the frequency by ten and outputs the $\bar{f}_c$ drive at a power of 2 mW. Voltage-controlled attenuators reduce the strength of the drive, which is broadcast from a room temperature horn through teflon lenses to a horn at 100 mK (Fig. 1.8) and enters the trap cavity through an inlet waveguide (Fig. 1.7).

Anomaly transitions are driven by potentials, oscillating near $\bar{\nu}_a$, applied to electrodes to drive off-resonant axial motion through the magnetic bottle gradient (Eq. 1.28). The gradient's $z\rho\hat{\boldsymbol{\rho}}$ term mixes the driven oscillation of z at $\bar{\nu}_a$ with that of ρ at $\bar{f}_c$ to produce an oscillating magnetic field perpendicular to **B** as needed to flip the spin. The axial amplitude required to produce the desired transition probability is too small to affect the lineshape (Sect. 1.5.4); nevertheless, we apply a detuned drive of the same strength during cyclotron attempts so the electron samples the same magnetic gradient.

Quantum jump spectroscopy of each resonance follows the same procedure. With the electron prepared in the spin-up ground state $\left|0, \frac{1}{2}\right\rangle$, the magnetron radius is reduced with 1.5 s of strong sideband cooling at $\bar{\nu}_z + \bar{\nu}_m$ with the SEO turned off immediately and the detection amplifiers turned off after 0.5 s. After an additional 1 s to allow the axial motion to thermalize with the tuned circuit, we apply a 2 s pulse of either a cyclotron drive near $\bar{f}_c$ or an anomaly drive near $\bar{\nu}_z$ with the other drive applied simultaneously but detuned far from resonance. The detection electronics and SEO are turned back on; after waiting 1 s to build a steady-state axial amplitude, we measure $\bar{\nu}_z$ and look for a 20 ppb shift up (from a cyclotron transition) or down (from an anomaly transition followed by a spontaneous decay to $\left|0, -\frac{1}{2}\right\rangle$) in frequency. Cavity-inhibited spontaneous emission provides the time needed to observe cyclotron transitions before decay. The several-cyclotron-lifetimes wait for a spontaneous decay after an anomaly attempt is the rate-limiting step in the spectroscopy. After a successful anomaly transition and decay, simultaneous cyclotron and anomaly drives pump the electron back to $\left|0, \frac{1}{2}\right\rangle$. All timing is done in hardware. We probe each resonance line with discrete excitation attempts spaced in frequency by approximately 10 % of the linewidth. We step through each drive frequency on the $\bar{f}_c$ line, then each on the $\bar{\nu}_a$ line, and repeat.

1.5.2 The Electron as Magnetometer

Slow drifts of the magnetic field are corrected using the electron itself as a magnetometer. Accounting for these drifts allows the combination of data taken over many days, giving a lineshape signal-to-noise that allows the systematic investigation of lineshape uncertainties at each field. For a half-hour at the beginning and end of a run and again every three hours throughout, we alter our cyclotron spectroscopy routine by applying a stronger drive at a frequency below $\bar{f}_c$. Using the same timing as above but a ten-times-finer frequency step, we increase the drive frequency until observing a successful transition. We then jump back 60 steps and begin again.

We model the magnetic field drift by fitting a polynomial to these "edge" points (so-called because the ideal cyclotron lineshape has a sharp low-frequency edge). Since we time-stamp every cyclotron and anomaly attempt, we use the smooth curve to remove any field drift. This edge-tracking adds a 20 % overhead, but allows the use of data from nights with a larger than usual field drift, and the combination of data from different nights.

1.5.3 Measuring the Axial Frequency

In addition to $\bar{f}_c$ and $\bar{\nu}_a$, measuring $g/2$ requires a determination of the axial frequency $\bar{\nu}_z$ (Eq. 1.19). To keep the relative uncertainty in $g/2$ from $\bar{\nu}_z$ below 0.1 ppt, we must know $\bar{\nu}_z$ to better than 50 ppb (10 Hz). This is easily accomplished. We routinely measure $\bar{\nu}_z$ when determining the cyclotron and spin states. However, the large self-excited oscillation amplitude in the slightly anharmonic axial potential typically results in a 10 ppb shift, compared to the $\bar{\nu}_z$ for the thermally-excited amplitude during the cyclotron and anomaly pulses. We cannot directly measure the axial frequency under the pulse conditions because the amplifiers are off. We come close when measuring $\bar{\nu}_z$ with the amplifiers on and all axial drives off. This thermal axial resonance appears as a dip on the amplifier noise resonance [50], and we use it as our measurement. The difference in $\bar{\nu}_z$ with the amplifiers on and off is negligible. A second shift comes from the interaction between the axial motion and the amplifier, which both damps the motion and shifts $\bar{\nu}_z$. The maximum shift of $\bar{\nu}_z$ is 1/4 of the damping rate, which at $\approx$1 ppb is negligible at our current precision. A third shift of $\bar{\nu}_z$ comes from the anomaly drive, which induces both a frequency-pulling from the off-resonant axial force and a Paul-trap shift from the change in effective trapping potential [54]; based on extrapolation from measured shifts at higher powers, we estimate these shifts combine to 1 ppb at the highest anomaly power used for the measurement—too small to affect $g/2$.

1.5.4 Frequencies from Lineshapes

The cyclotron frequency $\bar{f}_c$ and anomaly frequency $\bar{\nu}_a$ (Fig. 1.6) must be determined from their respective quantum jump spectroscopy lineshapes (Fig. 1.11). The observed lineshapes are much broader than the natural linewidth that arises because the excited cyclotron state decays by the cavity-inhibited spontaneous emission of synchrotron radiation. The shape arises because the electron experiences a magnetic field that varies during the course of a measurement. Variations arise because of the electron's thermal axial motion within the magnetic bottle gradient, for example. Other possible variations could arise because the magnetic field for the Penning trap fluctuates in time, or because of a distribution of magnetron orbit sizes for the quantum jump trials.

Once the slow drift of the magnetic field (p. 24) has been removed, there is no reason for the electron to sample a different distribution of magnetic field values while the anomaly frequency is being measured compared to when the trap-modified cyclotron frequency is being measured. Each resonance shape converts the distribution of sampled magnetic fields values into the corresponding distribution of frequency values. Dividing the quantum jump lineshapes into frequency bins, we obtain average cyclotron and anomaly frequencies by weighting the frequency of each bin by the number of quantum jumps in the bin, and use these average frequencies in Eq. 1.19.

Using the weighted average frequencies will remove shifts to $g/2$ caused by the thermal axial motion of the electron within the magnetic bottle gradient, the largest source of the observed linewidth. The use of weighted average frequencies should also account for temporal fluctuations in the magnetic field of the Penning trap on the measurement time scale for the frequencies. If there is a distribution of magnetron radii for the quantum jump trials, the weighted average method should account for the resulting distribution of magnetic field values as well.

To verify the weighted averages method, and to assign safe uncertainties to the average frequencies that we deduce using it, we also analyze our measured lineshapes in a very different way. We start with an analytic calculation of the lineshape for thermal Brownian motion of the axial motion for a given axial temperature T_z [55]. We then fit the measured cyclotron and anomaly lineshapes (Fig. 1.11) to the ideal lineshape convolved with a Gaussian broadening function to take into account other sources of the magnetic field distribution. The analytically calculated lineshapes are the dashed curves in Fig. 1.11, the maximum-likelihood fits to the broadened lineshapes are solid curves, and the gray bands indicate where we would expect 68 % of the measured points to lie. The insets to Fig. 1.11 show the best-fit resolution functions. We assign a lineshape uncertainty that is the size of the differences between the $g/2$ value determined from the fitting and our preferred weighted averages method.

The linewidths are wider for two of the four measurements in Fig. 1.11, and they remained reproducible over the weeks required to take each data point. A wider cyclotron linewidth indicates a higher axial temperature. We know of no reason that the axial temperatures should be different for different values of the Penning trap field;

this is one reason that we assign the larger uncertainties that reflect the difference between the two methods. The narrower lineshapes have better agreement between the weighted average method and the fit method, and hence the assigned lineshape uncertainties are smaller. Not surprisingly, the narrower lines better determine the corresponding frequencies.

For the 2008 measurement the lineshape uncertainty is larger than any other. Future efforts will focus upon understanding and reducing the lineshape broadening and uncertainty.

1.5.5 Cavity Shifts

Despite the precision reached in this measurement, only one correction to the directly measured $g/2$ value is required, the $\Delta g_{cav}/2$ included in Eq. 1.19. The correction is a cavity shift correction that depends upon interaction of the electron with nearby cavity radiation modes. The trap cavity modifies the density of states of the radiation modes of free space, though not enough to significantly affect QED calculations of g [56]. Since the cavity shift correction depends upon the electron cyclotron frequency, we measure $g/2$ at four different cyclotron frequencies to make sure that the same $g/2$ is deduced when cavity shifts of different sizes are applied.

The cavity-inhibited spontaneous emission narrows the cyclotron resonance line, giving the time in the excited state that is needed to turn on the self-excited oscillator, and to average its signal long enough determine the cyclotron state. Cavity shifts are the unfortunate downside of the cavity, arising because the cyclotron oscillator has its frequency pulled by its coupling to nearby radiation modes of the cavity.

The cylindrical Penning trap was invented to make a microwave cavity with a calculable geometry. Section 1.3.2 describes a perfect cylindrical trap cavity and the radiation fields that it can support. However, the trap is not perfectly machined, it changes its size as it cools from room temperature down to 0.1 K, and it has small slits that make it possible to bias sections to form a Penning trap.

The shape of the radiation fields near the center of the trap cavity are not greatly altered for the real cavity, but the resonant frequencies of the modes are slightly shifted. The frequency shifts are not enough to keep us from identifying most modes by comparing to calculated frequencies, but are large enough that we must measure the mode frequencies if we are to characterize the interaction of the cavity and an electron. The mode quality factors (resonant frequencies divided by energy damping rates) must also be determined. The decay of the radiation field within the cavity depends upon power dissipated by currents (induced in the electrodes and modified by the slits), and upon the loss of microwave power that escapes the trap despite the choke flanges in the slits.

We developed two methods to learn the resonant frequencies of the radiation modes of real trap cavity.

1. A cloud of electrons near the center of the trap is heated using a parametric driving force. The electrons cool via synchrotron radiation with a rate that is highest when their cyclotron frequency is resonant with a cavity radiation mode, and that is very small far from resonance [32–34, 57]. Figure 1.12a shows the peaks in the signal from the electrons that correspond to resonance with cavity radiation modes that are labeled as described earlier.
2. The measured spontaneous emission rate for a single electron near the center of the trap cavity (Fig. 1.12b), and the dependence of this rate upon the amplitude of the axial oscillation of the electron (Fig. 1.12c), both depend upon the proximity of the electron cyclotron frequency to cavity radiation modes that couple to a nearly centered electron. Figure 1.13 illustrates how the one-electron damping rate and dependence upon axial oscillation amplitude are measured.

From the cavity spectra in Fig. 1.12a–c we deduce the mode frequencies and uncertainties represented by the gray bands in these figures. Our identification of the modes is aided by several features of the spectra. Modes that are strongly coupled to the electrons (the coupling increases with electron number) can split into two normal modes. A large axial oscillation during measurements of the cavity spectrum produces sidebands at the axial frequency for modes with a node at the trap center, and at twice the sidband frequency for radiation modes with an antinode at the center. Modes which would not couple to a perfectly centered electron will couple more strongly to the electrons as their number is increased so that they occupy a larger volume. From 2006 to 2008 our understanding of the cavity improved when we became aware of and were able to measure a small displacement of the electrostatic center of the trap (where the electron resides), and the center for the cavity radiation modes.

So far we have used the calculable cylindrical trap geometry to know which radiation modes can couple to an electron near the center of the trap, and we have recognized these modes in measured cavity spectra by comparing their measured frequencies to what is calculated for a perfect cavity. Next we use the measured radiation mode frequencies and quality factors as input to a calculation of the cavity shift of the electron cyclotron frequency as a function of the electron cyclotron frequency (Fig. 1.12d).

A calculation of the shifts [55, 58] must carefully distinguish and remove the electron self-energy from the electron-cavity interaction. The uncertainty in the measured inputs give a cavity shift uncertainty (Fig. 1.12e) that is small between the resonance frequencies of modes that couple strongly to a centered electron, and then increases strongly closer to the resonant frequencies of these modes. The diamonds at the top of the figure show how in our four measurements of $g/2$ we avoid the electron cyclotron frequencies for which the uncertainty is the largest. Figure 1.14 shows the good agreement attained between the four measurements when the cavity shifts are applied.

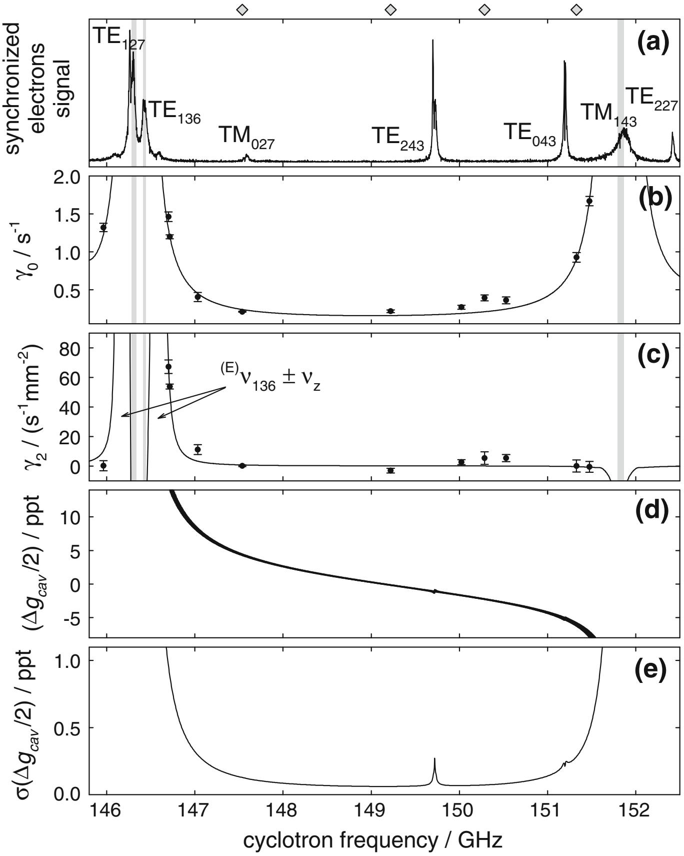

Fig. 1.12 Cavity shift results come from synchronized electrons (**a**) and from direct measurements with one electron of γ_c (**b**) and its dependence on axial amplitude (**c**). Together, they provide uncertainties in the frequencies of coupled cavity radiation modes (*gray*) that translate into an uncertainty band of cavity shifts $\Delta g_{cav}/2$ (**d**) whose half-width, i.e., the cavity shift uncertainty, is plotted in (**e**). The diamonds at the top indicate the cyclotron frequencies of the four $g/2$ measurements

1.6 Results and Applications

1.6.1 Most Accurate Electron $g/2$

The measured values, shifts, and uncertainties for the four separate measurements of $g/2$ are in Table 1.2. The uncertainties are lower for measurements with smaller cavity shifts and smaller linewidths, as might be expected. Uncertainties for variations of the power of the $\bar{\nu}_a$ and $\bar{f}_c$ drives are estimated to be too small to show up in the table. A weighted average of the four measurements, with uncorrelated and correlated errors combined appropriately, gives the electron magnetic moment in Bohr magnetons,

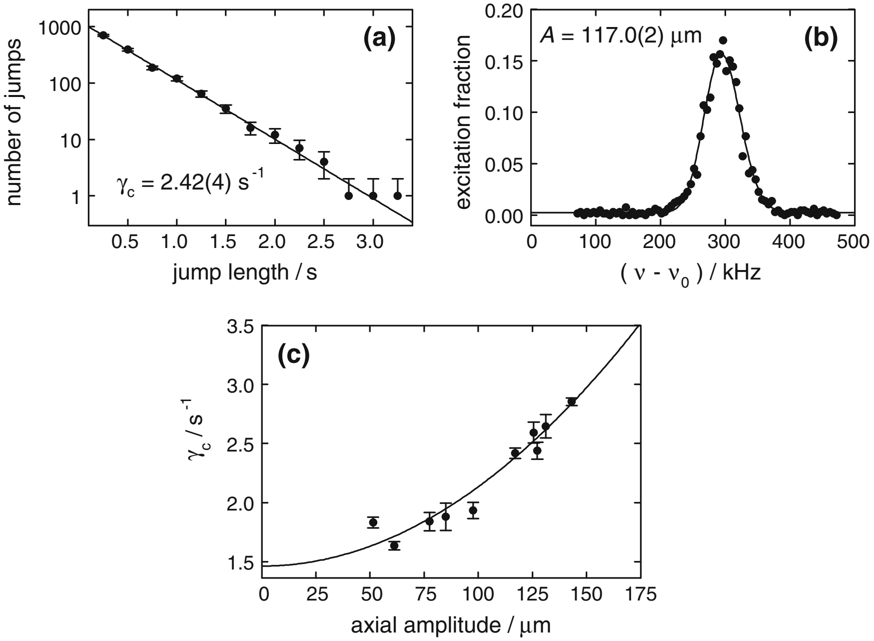

Fig. 1.13 Measurement of the cyclotron damping rate at 146.70 GHz, near the upper sideband of TE_{136}. The cyclotron damping rate as a function of axial amplitude (**c**) extrapolates to the desired lifetime. Each point in (**c**) consists of a damping rate measured from a fit to a histogram of cyclotron jump lengths (**a**) as well as an axial amplitude measured from a driven *cyclotron line* (**b**)

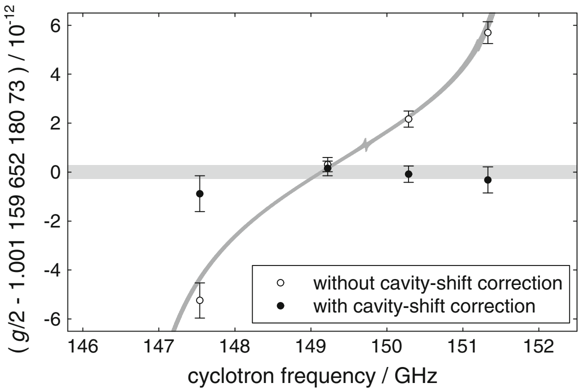

Fig. 1.14 Four measurements of $g/2$ without (*open*) and with (*filled*) cavity-shift corrections. The *light gray* uncertainty band shows the average of the corrected data. The *dark gray* band indicates the expected location of the uncorrected data given our result in Eq. 1.1 and including only the cavity-shift uncertainty

Table 1.2 Measurements and shifts with uncertainties multiplied by 10^{12}

$\bar{f}_c$	147.5 GHz	149.2 GHz	150.3 GHz	151.3 GHz
$g/2$ raw	−5.24(0.39)	0.31 (0.17)	2.17 (0.17)	5.70 (0.24)
Cav. shift	4.36(0.13)	−0.16 (0.06)	−2.25 (0.07)	−6.02 (0.28)
Lineshape				
correlated	(0.24)	(0.24)	(0.24)	(0.24)
uncorrelated	(0.56)	(0.00)	(0.15)	(0.30)
$g/2$	−0.88(0.73)	0.15 (0.30)	−0.08 (0.34)	−0.32 (0.53)

The cavity-shifted "$g/2$ raw" and corrected "$g/2$" are offset from our result in Eq. 1.1

$$\mu/\mu_B = -g/2 = -1.001\,159\,652\,180\,73\,(28) \quad [0.28\text{ ppt}]. \tag{1.1}$$

The uncertainty is 2.7 and 15 times smaller than the 2006 and 1987 measurements, and 2,300 times smaller than has been achieved for the heavier muon lepton [59].

1.6.2 Most Accurate Determination of α

The new measurement determines the fine structure constant, $\alpha = e^2/(4\pi\varepsilon_0\hbar c)$, much more accurately than does any other method. The fine structure constant is the fundamental measure of the strength of the electromagnetic interaction in the low energy limit, and it is also a crucial ingredient of our system of fundamental constants [60]. Only the bare essentials of what is needed to determine α from $g/2$ are summarized here.

The standard model relates g and α by

$$\begin{aligned}\frac{g}{2} = {} & 1 + C_2\left(\frac{\alpha}{\pi}\right) + C_4\left(\frac{\alpha}{\pi}\right)^2 + C_6\left(\frac{\alpha}{\pi}\right)^3 + C_8\left(\frac{\alpha}{\pi}\right)^4 \\ & + C_{10}\left(\frac{\alpha}{\pi}\right)^5 + \cdots + a_{\text{hadronic}} + a_{\text{weak}},\end{aligned} \tag{1.31}$$

with the asymptotic series and the values of the C_k coming from QED. Very small hadronic and weak contributions are included, along with the assumption that there is no significant modification from electron substructure or other physics beyond the standard model (Fig. 1.15).

QED calculations give the constants C_k,

$$C_2 = 0.500\,000\,000\,000\,00 \text{ (exact)} \tag{1.32}$$

$$C_4 = -0.328\,478\,444\,002\,55\,(33) \tag{1.33}$$

$$C_6 = 1.181\,234\,016\,816\,(10) \tag{1.34}$$

$$C_8 = -1.909\,7\,(20) \tag{1.35}$$

$$C_{10} = 9.16\,(0.57). \tag{1.36}$$

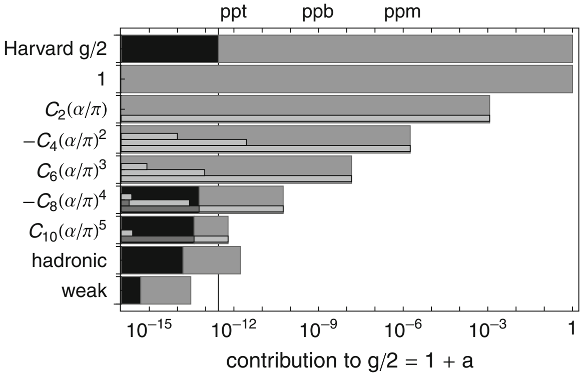

Fig. 1.15 Contributions to $g/2$ for the experiment (*top bar*), terms in the QED series (*below*), and from small distance physics (*below*). Uncertainties are *black*. The inset *light gray bars* represent the magnitude of the larger mass-independent terms (A_1) and the smaller A_2 terms that depend upon either m_e/m_μ or m_e/m_τ. The even smaller A_3 terms, functions of both mass ratios, are not visible on this scale

The QED theory for C_2 [61], C_4 [62–64], and C_6 [65] is exact, with no uncertainty, except for an essentially negligible uncertainty in C_4 and C_6 that comes from a weak functional dependence upon the lepton mass ratios, m_μ/m_e and m_τ/m_e. Numerical QED calculations give the value and uncertainty for C_8 and C_{10} [6]. The first evaluation of C_{10} is the most significant theoretical advance since the electron magnetic moment was measured. A remarkable 12,672 Feynman diagrams are involved.

The hadronic anomaly a_{hadronic}, calculated within the context of the Standard Model,

$$a_e^{\text{hadronic}} = 1.678(15) \times 10^{-12}\,, \tag{1.37}$$

contributes at the level of several times the current experimental uncertainty, but the calculation uncertainty in the hadronic anomaly is not important [66–69]. The weak anomaly is negligible for the current experimental precision.

The most accurately determined fine structure constant is given by

$$\begin{aligned} \alpha^{-1} &= 137.035\,999\,173\,(33)\,(8) \quad [0.24\text{ ppb}]\,[0.06\text{ ppb}], \\ &= 137.035\,999\,173\,(34) \quad [0.25\text{ ppb}]. \end{aligned} \tag{1.38}$$

The first line shows that the 0.24 ppb experimental uncertainty (33) is larger than the 0.06 ppb theoretical uncertainty (8) now that C_{10} has been calculated. The theory uncertainty contribution to α is divided as (7) and (5) for C_8 and C_{10}. The uncertainties from the experiment and theory are represented in Fig. 1.16. The dashes show the uncertainties before the recent theoretical advances.

The total 0.25 ppb uncertainty in α is nearly three times smaller than the 0.66 ppm uncertainty for the next most precise determination [7] (Fig. 1.2). The so-called atom recoil determination that is used actually requires measurements of the Rydberg

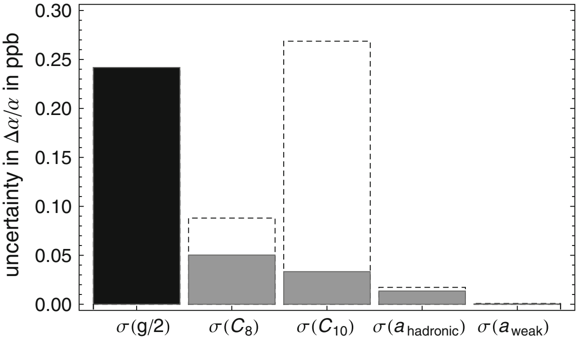

Fig. 1.16 Experimental uncertainty (*black*) and theoretical uncertainties (*gray*) that determine the uncertainty in the α that is determined from the measured electron $g/2$. The dashes present the uncertainties before the very recent theoretical advances

constant [70, 71], transition frequencies [7, 72], mass ratios [73–75], and either a Rb [7] or Cs [76] recoil velocity measured in an atom interferometer.

1.6.3 Testing the Standard Model and QED

The dimensionless electron magnetic moment g that is measured can be compared to the $g(\alpha)$ that is predicted by the Standard Model of particle physics. The input needed to calculate $g(\alpha)$ is the measured fine structure constant α (that is determined without the use of the electron magnetic moment). The most accurately measured and calculated values of $g/2$ are currently given by

$$g/2 = 1.001\ 159\ 652\ 180\ 73\ (28)\ [0.28\ \text{ppt}], \tag{1.39}$$

$$g(\alpha)/2 = 1.001\ 159\ 652\ 181\ 78\ (77)\ [0.77\ \ \text{ppt}]. \tag{1.40}$$

The measurement is our one-electron quantum cyclotron measurement [2]. The calculated value $g(\alpha)/2$ comes from using the most precise Rb value of α [7] in Eq. 1.31. The uncertainty in this “calculated” value actually comes almost entirely from the uncertainty in the Rb α. The Standard Model prediction is thus tested and verified to 0.8 ppt. The smaller 0.3 ppt uncertainty in the measured $g/2$, along with the comparable uncertainty in the QED calculation, would allow a better test of QED if a more precise, independent value of α could be measured.

About 1 part per thousand of the electron $g/2$ comes from the unavoidable interaction of the electron with the virtual particles of “empty space”, as described by quantum electrodynamics (QED) and represented in Fig. 1.17. Where testing QED is the primary focus, measured and calculated values of the so-called anomalous magnetic moment of the electron (defined by $a = g/2 - 1$ so that the Dirac contribution

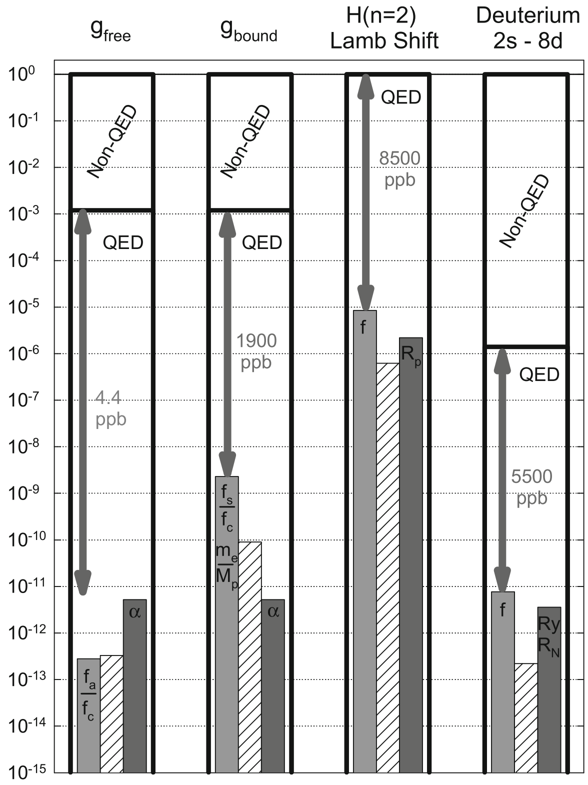

Fig. 1.17 Comparisons of precise tests of QED. The arrows represent the fractional accuracy to which the QED contribution to the measured g values and frequencies that are measured

is subtracted out) are often compared. The measured and calculated values of a that correspond to the $g/2$ values above are

$$a = 0.001\ 159\ 652\ 180\ 73\ (\ 28)\ [0.24\ \text{ppb}], \tag{1.41}$$

$$a(\alpha) = 0.001\ 159\ 652\ 181\ 78\ (\ 77)\ [0.66\ \ \text{ppb}], \tag{1.42}$$

At the one standard deviation level, the difference of the measured and calculated values is

$$\delta a = a - a(\alpha) \tag{1.43}$$

$$= g/2 - g(\alpha)/2 \tag{1.44}$$

$$= 1.05(0.82) \times 10^{-12}. \tag{1.45}$$

The possible difference between the measurement and calculation is thus bounded by

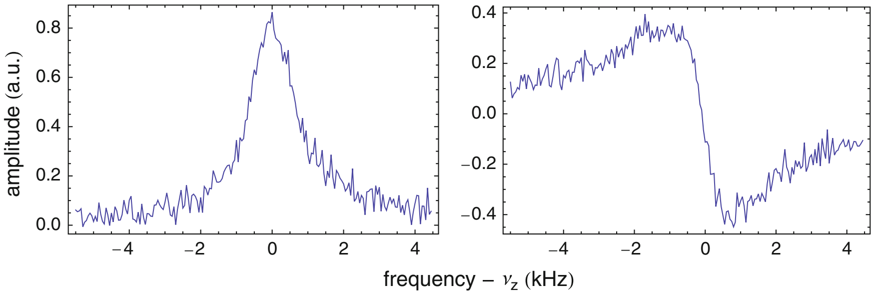

Fig. 1.18 A driven resonance for positrons captured and stored next to a Penning trap designed for a new generation of electron and posiron magnetic moment measurements

$$|\delta a| < 1.9 \times 10^{-12}, \tag{1.46}$$

at the one standard deviation level, with this bound arising almost entirely from the uncertainty in the measurement of α from Rb.

Some of the most precise tests of bound-state QED are compared in Fig. 1.18 with the electron $g/2$. The QED test based upon the measurements [74] and calculation [77] of $g/2$ for an electron bound in an ion tests QED less precisely. In fact, the calculated value of the bound g values depends upon the mass of the electron strongly enough that this measurement is now being used to determine the electron mass in amu, much as we determine α from our measurements of the magnetic moment of the free electron. The $\mathrm{n} = 2$ Lamb shift in hydrogen is essentially entirely due to QED. However, the measurements are much less precise so that QED is again tested less precisely.

The last example in the figure is a QED test based upon a number of measurements of hydrogen and deuterium transition frequencies—the QED contribution to which are typically at the ppm level. Theoretical calculations that depend upon the Rydberg constant, the fine structure constant, the ratio of the electron and proton masses and the size of the nucleus are fit to a number of accurately measured transition frequencies for hydrogen and deuterium. The fit determines values for the mentioned constants. The QED test come from removing one of the measured lines from the fit, and using the best fit to predict the value of the transition frequency that was omitted. This process tests the Standard Model prediction at a comparable precision to that provided using the magnetic moment of the electron. However, it tests the size of the QED contribution to a much lower fractional precision.

The QED tests described so far test QED predictions to the highest precision and the highest order in α. There are many other tests of QED with a much lower precision. Although these tests are outside of the scope of this work it is worth mentioning that it is interesting to probe QED in other ways. For example, it seems interesting to test QED for systems whose binding energy is very large, even comparable to the electron rest mass energy as can be done in high Z systems. Another example is probing the QED of positronium, the bound state of an electron and a positron, insofar as annihilation and exchange effects are quite different than what must be calculated for normal atoms.

1.6.4 Probe for Electron Substructure

Comparing experiment and theory probes for possible electron substructure at an energy scale one might only expect from a large accelerator. An electron whose constituents would have mass $m^* \gg m$ has a natural size scale, $R = \hbar/(m^* c)$. The simplest analysis of the resulting magnetic moment [78] gives $\delta a \sim m/m^*$, suggesting that $m^* > 260{,}000\,\mathrm{TeV}/c^2$ and $R < 9 \times 10^{-25}\,\mathrm{m}$. This would be an incredible limit, since the largest e^+e^- collider (LEP) probed for a contact interaction at an $E = 10.3\,\mathrm{TeV}$ [79], with $R < (\hbar c)/E = 2 \times 10^{-20}\,\mathrm{m}$.

However, the simplest argument also implies that the first-order contribution to the electron self-energy goes as m^* [78]. Without heroic fine tuning (e.g., the bare mass cancelling this contribution to produce the small electron mass) some internal symmetry of the electron model must suppress both mass and moment. For example, a chirally invariant model [78], leads to $\delta a \sim (m/m^*)^2$. In this case, $m^* > 360\,\mathrm{GeV}/c^2$ and $R < 5 \times 10^{-19}\,\mathrm{m}$. These are stringent limits to be set with an experiment carried out at 100 mK, although they are not yet at the LEP limits. With a more precise measurement of α, so this was limited only by the experimental uncertainty in a, then we could set a limit $m^* > 1\,\mathrm{TeV}$ and $R < 2 \times 10^{-19}$.

1.6.5 Comparison to the Muon $g/2$

The electron $g/2$ is measured about 2300 times more accurately than is $g/2$ for its heavier muon sibling [2, 59]. Because the electron is stable there is time to isolate one electron, cool it so that it occupies a very small volume within a magnetic field, and to resolve the quantum structure in its cyclotron and spin motions. The short-lived muon must be studied before it decays in a very small fraction of a second, during which times it orbits in a very large orbit over which the same magnetic field homogeneity realized with a nearly motionless electron cannot be maintained.

Why then measure the muon $g/2$? The compelling reason is that the muon $g/2$ is expected to be more sensitive to physics beyond the standard model by about a factor of 4×10^4, which is the square of the ratio of the muon to the electron mass. In terms of Eq. 1.10 this means that a_{new} is expected to be bigger for the muon than for the electron by this large factor, making the muon a more attractive probe for new physics.

Unfortunately, the other Standard Model contribution, $a_{\mathrm{hadronic}} + a_{\mathrm{weak}}$, is also bigger by approximately the same large factor, rather than being essentially negligible as in the electron case. Correctly calculating these terms is a significant challenge to detecting new physics. These large terms, and the much lower measurement precision, also make the muon an unattractive candidate (compared to the electron) for determining the fine structure constant and for testing QED.

The measured electron $g/2$ makes two contributions to using the muon system for probing for physics beyond the Standard Model. Both relate to determining the muon QED anomaly $a_{\mathrm{QED}}(\alpha)$

1. The electron measurement of $g/2$ makes possible the most accurate determination of the fine structure constant (discussed in the previous section) as is needed to calculate $a_{\mathrm{QED}}(\alpha)$.
2. The electron measurement of $g/2$ and an independently measured value of α test QED calculations of the very similar $a_{\mathrm{QED}}(\alpha)$ terms in the electron system.

The QED contribution must be accurately subtracted from the measured muon $g-2$ if the much smaller possible contribution from new physics is to be observed.

1.7 Prospects and Conclusion

In conclusion, our 2008 measurement of the electron $g/2$ is 15 times more accurate than the 1987 measurement that provided $g/2$ and α for nearly 20 years, and 2.7 times more accurate than our 2006 measurement that superseded it.

With no uncertainty show-stoppers yet presenting themselves, an entirely new solenoid, dewar, and trap apparatus has been designed and constructed. Figure 1.18 shows the signals from positrons now being stored in the new apparatus. Achieving the reported electron $g/2$ uncertainty with a positron to make the most stringent lepton CPT test seems feasible.

We also intend to seek a much more precise measurement of the electron magnetic moment. Several experimental items warrant further study. First is the broadening of the expected lineshapes which limits the splitting of the resonance lines. Second, the variation in axial temperatures in the observed resonance lineshapes is not understood, and a larger uncertainty comes from the wider lineshapes. Third, cavity sideband cooling could cool the axial motion to near its quantum ground state for a more controlled measurement. Fourth, the new apparatus should be much less sensitive to vibration and other variations in the laboratory environment.

With QED and the assumption of no new physics beyond the standard model of particle physics, the new measurement determines α nearly three times more accurately than any independent method. Given the recent theoretical advance, a better measurement of the electron $g/2$ will produce a more precise value of α.

The measured $g/2$ and an independently measured α test QED and probe for electron size at an unprecedented precision. Prospects are good that better measurements will enable even more sensitive tests of the Standard Model.

Acknowledgments The electron magnetic moment measurements were supported by the atomic physics program of the NSF. The antiproton magnetic moment measurements and antihydrogen experiments were supported by the NSF and the AFOSR.

References

1. B. Odom, D. Hanneke, B. D'Urso, G. Gabrielse, New measurement of the electron magnetic moment using a one-electron quantum cyclotron. Phys. Rev. Lett. **97**, 030801 (2006)
2. D. Hanneke, S. Fogwell, G. Gabrielse, New measurement of the electron magnetic moment and the fine structure constant. Phys. Rev. Lett. **100**, 120801 (2008)
3. D. Hanneke, S. Fogwell Hoogerheide, G. Gabrielse, Cavity control of a single-electron quantum cyclotron: measuring the electron magnetic moment. Phys. Rev. A **83**, 052122 (2011)
4. B. Lautrup, H. Zinkernagel, g-2 and the trust in experimental results. Stud. Hist. Phil. Mod. Phys. **30**, 85–110 (1999)
5. R.S. Van Dyck, Jr., P.B. Schwinberg, H.G. Dehmelt, New high-precision comparison of electron and positron g factors. Phys. Rev. Lett. **59**, 26–29 (1987)
6. T. Aoyama, M. Hayakawa, T. Kinoshita, M. Nio, Quantum electrodynamics calculation of lepton anomalous magnetic moments: numerical approach to the perturbation theory of QED. Prog. Theor. Exp. Phys. **01A**, 107 (2012)
7. R. Bouchendira, P. Clade, S. da Guellati-Khe'lifa, F. Nez, F. Biraben, New determination of the fine structure constant and test of the quantum electrodynamics. Phys. Rev. Lett. **106**, 080801 (2011)
8. G. Gabrielse, A. Khabbaz, D.S. Hall, C. Heimann, H. Kalinowsky, W. Jhe, Precision mass spectroscopy of the antiproton and proton using simultaneously trapped particles. Phys. Rev. Lett. **82**, 3198–3201 (1999)
9. G. Gabrielse, Antiproton mass measurements. Int. J. Mass Spectrom. **251**, 273 (2006)
10. J. DiSciacca, M. Marshall, K. Marable, G. Gabrielse, and the ATRAP Collaboration, One-particle measurement of the antiproton magnetic moment. Phys. Rev. Lett. **110**, 130801 (2013)
11. J. DiSciacca, M. Marshall, K. Marable, G. Gabrielse, Resolving an individual one-proton spin flip to determine a proton spin state. Phys. Rev. Lett. **110**, 140406 (2013)
12. A. Mooser et al., Resolution of single spin flips of a single proton. Phys. Rev. Lett. **110**, 140405 (2013)
13. G. Gabrielse, Penning traps, masses and antiprotons, in *Fundamental Symmetries*, ed. by P. Bloch, P. Pavlopoulos, R. Klapisch (Plenum, New York, 1987), pp. 59–75
14. G. Gabrielse, X. Fei, K. Helmerson, S.L. Rolston, R.L. Tjoelker, T.A. Trainor, H. Kalinowsky, J. Haas, W. Kells, First capture of antiprotons in a penning trap: a keV source. Phys. Rev. Lett. **57**, 2504–2507 (1986)
15. G. Gabrielse, N.S. Bowden, P. Oxley, A. Speck, C.H. Storry, J.N. Tan, M. Wessels, D. Grzonka, W. Oelert, G. Schepers, T. Sefzick, J. Walz, H. Pittner, T.W. Hänsch, E.A. Hessels, Background-free observation of cold antihydrogen with field-ionization analysis of its states. Phys. Rev. Lett. **89**, 213401 (2002)
16. G. Gabrielse, N.S. Bowden, P. Oxley, A. Speck, C.H. Storry, J.N. Tan, M. Wessels, D. Grzonka, W. Oelert, G. Schepers, T. Sefzick, J. Walz, H. Pittner, T.W. Hänsch, E.A. Hessels, Driven production of cold antihydrogen and the first measured distribution of antihydrogen states. Phys. Rev. Lett. **89**, 233401 (2002)
17. M. Amoretti et al., Production and detection of cold antihydrogen atoms. Nature **419**, 456–459 (2002)
18. Y. Enomoto et al., Phys. Rev. Lett. **105**, 243401 (2010)
19. E.A. Hessels, D.M. Homan, M.J. Cavagnero, Two-stage Rydberg charge exchange: an efficient method for production of antihydrogen. Phys. Rev. A **57**, 1668–1671 (1998)
20. A. Speck, C.H. Storry, E.A. Hessels, G. Gabrielse, Laser-controlled production of Rydberg positronium via charge exchange collisions. Phys. Lett. B **597**, 257–262 (2004)
21. G.B. Andresen et al., Confinement of antihydrogen for 1000 seconds. Nature Phys. **7**, 558–564 (2011).
22. G. Gabrielse, R. Kalra, W.S. Kolthammer, R. McConnell, P. Richerme, D. Grzonka, W. Oelert, T. Sefzick, M. Zielinski, D.W. Fitzakerley, M.C. George, E.A. Hessels, C.H. Storry, M. Weel, A. Müllers, J. Walz, Trapped antihydrogen in its ground state. Phys. Rev. Lett. **108**, 113002 (2012)

23. A. Rich, J.C. Wesley, Current status of the lepton g factors. Rev. Mod. Phys. **44**, 250–283 (1972)
24. R.S. Van Dyck, Jr., P.B. Schwinberg, H.G. Dehmelt, The Electron (Kluwer Academic Publishers, The Netherlands, 1991), pp. 239–293
25. L.S. Brown, G. Gabrielse, Geonium theory: physics of a single electron or ion in a penning trap. Rev. Mod. Phys. **58**, 233–311 (1986)
26. L.S. Brown, G. Gabrielse, Precision spectroscopy of a charged particle in an imperfect penning trap. Phys. Rev. A **25**, 2423–2425 (1982)
27. G. Gabrielse, F. Colin MacKintosh, Cylindrical penning traps with orthogonalized anharmonicity compensation. Int. J. Mass Spec. Ion Proc. **57**, 1–17 (1984)
28. J.N. Tan, G. Gabrielse, One electron in an orthogonalized cylindrical penning trap. Appl. Phys. Lett. **55**, 2144–2146 (1989)
29. G. Gabrielse, Relaxation calculation of the electrostatic properties of compensated penning traps with hyperbolic electrodes. Phys. Rev. A **27**, 2277–2290 (1983)
30. L.S. Brown, G. Gabrielse, J.N. Tan, K.C.D. Chan, Cyclotron motion in a penning trap microwave cavity. Phys. Rev. A **37**, 4163–4171 (1988)
31. J.D. Jackson, *Classical Electrodynamics*, 2nd edn. (Wiley, New York, 1975)
32. J. Tan, G. Gabrielse, Synchronization of parametrically pumped electron oscillators with phase bistability. Phys. Rev. Lett. **67**, 3090–3093 (1991)
33. J.N. Tan, G. Gabrielse, Parametrically-pumped electron oscillators. Phys. Rev. A **48**, 3105 (1993)
34. G. Gabrielse, J.N. Tan, L.S. Brown, Cavity shifts of measured electron magnetic moments (World Scientific, Singapore, 1990), pp. 389–418
35. G. Gabrielse, X. Fei, L.A. Orozco, R.L. Tjoelker, J. Haas, H. Kalinowsky, T.A. Trainor, W. Kells, Thousand-fold improvement in the measured antiproton mass. Phys. Rev. Lett. **65**, 1317–1320 (1990)
36. G. Gabrielse, J. Tan, Self-shielding superconducting solenoid systems. J. Appl. Phys. **63**, 5143–5148 (1988)
37. G. Gabrielse, J.N. Tan, L.A. Orozco, S.L. Rolston, C.H. Tseng, R.L. Tjoelker, A superconducting solenoid system which cancels fluctuations in the ambient magnetic field. J. Mag. Res. **91**, 564–572 (1991)
38. E.S. Meyer, I.F. Silvera, B.L. Brandt, Eddy current shielding and heating: reduction of dissipation for very low—temperature experiments in the presence of magnetic field ripple. Rev. Sci. Instrum. **60**, 2964–2968 (1989)
39. D.F. Phillips, A precision comparison of the $\bar{p} - p$ charge-to-mass ratios, Ph.D. thesis (Harvard University, Cambridge, 1996)
40. R.S. Van Dyck, Jr., D.L. Farnham, S.L. Zafonte, P.B. Schwinberg, Ultrastable superconducting magnet system for a Penning trap mass spectrometer. Rev. Sci. Instrum. **70**, 1665–1671 (1999)
41. B. Odom, Fully quantum measurement of the electron magnetic moment, Ph.D. thesis (Harvard University, Cambridge, 2004)
42. G. Gabrielse, H. Dehmelt, Observation of inhibited spontaneous emission. Phys. Rev. Lett. **55**, 67–70 (1985)
43. S. Peil, G. Gabrielse, Observing the quantum limit of an electron cyclotron: QND measurements of quantum jumps between fock states. Phys. Rev. Lett. **83**, 1287–1290 (1999)
44. K.S. Thorne, R.W.P. Drever, C.M. Caves, Quantum nondemolition measurement of harmonic oscillators. Phys. Rev. Lett. **40**(11), 667–670 (1978)
45. V.B. Braginsky, F. Ya, Khalili, Quantum nondemolition measurements: the route from toys to tools. Rev. Mod. Phys. **68**(1–11), 1 (1996)
46. B. D'Urso, Cooling and self-excitation of a one-electron oscillator, Ph.D. thesis (Harvard University, Cambridge, 2003)
47. R. Van Dyck, Jr., P. Ekstrom, H. Dehmelt, Axial, magnetron, cyclotron and spin-cyclotron-beat frequencies measured on single electron almost at rest in free space (geonium). Nature **262**, 776 (1976)

48. B. D'Urso, B. Odom, G. Gabrielse, Feedback cooling of a one-electron oscillator. Phys. Rev. Lett. **90**(4), 043001 (2003)
49. B. D'Urso, R. Van Handel, B. Odom, D. Hanneke, G. Gabrielse, Single-particle self-excited oscillator. Phys. Rev. Lett. **94**, 113002 (2005)
50. D.J. Wineland, H.G. Dehmelt, Principles of the stored ion calorimeter. J. Appl. Phys. **46**, 919–930 (1975)
51. R. Kubo, The fluctuation-dissipation theorem. Rep. Prog. Phys. **29**(1), 255–284 (1966)
52. E.M. Purcell, Spontaneous emission probabilities at radio frequencies. Phys. Rev. **69**, 681 (1946)
53. D. Kleppner, Inhibited spontaneous emission. Phys. Rev. Lett. **47**, 233 (1981)
54. F.L. Palmer, Excitation of spin flips in geonium at small cyclotron quantum numbers: transition rates and frequency shifts. Phys. Rev. A **47**, 2610 (1993)
55. L.S. Brown, Geonium lineshape. Ann. Phys. (N.Y.), 159:62–98 (1985)
56. D.G. Boulware, L.S. Brown, T. Lee, Apparatus-dependent contributions to $g-2$?. Phys. Rev. D **32**, 729–735 (1985)
57. G. Gabrielse, J.N. Tan, One electron in a cavity (Academic Press, New York, 1994), pp. 267–299
58. L.S. Brown, Line shape for a precise measurement of the electron's magnetic moment. Phys. Rev. Lett. **52**, 2013–2015 (1984)
59. G.W. Bennett et al., Final report of the e821 muon anomalous magnetic moment measurement at BNL. Phys. Rev. D **73**, 072003 (2006)
60. P.J. Mohr, B.N. Taylor, D.B. Newell, Codata recommended values of the fundamental physical constants: 2010. Rev. Mod. Phys. **84**, 1527 (2012)
61. J. Schwinger, On quantum-electrodynamics and the magnetic moment of the electron. Phys. Rev. **73**, 416–417 (1948)
62. A. Petermann, Fourth order magnetic moment of the electron. Helv. Phys. Acta **30**, 407–408 (1957)
63. C.M Sommerfield, Magnetic dipole moment of the electron. Phys. Rev. **107**, 328–329 (1957)
64. C.M. Sommerfield, The magnetic moment of the electron. Ann. Phys. (N.Y.) **5**, 26–57 (1958)
65. S. Laporta, E. Remiddi, Analytical value of the electron $(g-2)$ at order a^3 in QED. Phys. Lett. B **379**, 283–291 (1996)
66. P.J. Mohr, B.N. Taylor, CODATA recommended values of the fundamental physical constants: 2002. Rev. Mod. Phys. **77**, 1–107 (2005)
67. A. Czarnecki, B. Krause, W.J. Marciano, Electroweak corrections to the muon anomalous magnetic moment. Phys. Rev. Lett. **76**, 3267–3270 (1996)
68. J. Prades, E. de Rafael, A. Vainshtein, *Hadronic Light-by-Light Scattering Contribution to the Muon Anomalous Magnetic Moment, chapter Hadronic Light-by-Light Scattering Contribution to the Muon Anomalous Magnetic Moment* (World Scientific, Singapore, 2009)
69. D. Nomura, T. Teubner, Hadronic contributions to the anomalous magnetic moment of the electron and the hyperfine splitting of muonium. Nucl. Phys. B **867**, 236 (2013)
70. Th Udem, A. Huber, B. Gross, J. Reichert, M. Prevedelli, M. Weitz, T.W. Hänsch, Phase-coherent measurement of the hydrogen $S-2S$ transition frequency with an optical frequency interval divider chain. Phys. Rev. Lett. **79**, 2646–2649 (1997)
71. C. Schwob, L. Jozefowski, B. de Beauvoir, L. Hilico, F. Nez, L. Julien, F. Biraben, O. Acef, J.J. Zondy, A. Clairon, Optical frequency measurement of the 2S–12D transitions in hydrogen and deuterium: rydberg constant and lamb shift determinations. Phys. Rev. Lett. **82**, 4960–4963 (1999)
72. V. Gerginov, K. Calkins, C.E. Tanner, J.J. McFerran, S. Diddams, A. Bartels, L. Hollberg, Optical frequency measurements of $6s^2S_{1/2} - 6p^2P_{1/2}(D_1)$ transitions in ^{133}Cs and their impact on the fine structure constant. Phys. Rev. A **73**, 032504 (2006)
73. M.P. Bradley, J.V. Porto, S. Rainville, J.K. Thompson, D.E. Pritchard, Penning trap measurements of the masses of ^{133}Cs, ^{87,85}Rb, and ^{23}Na with uncertainties ≤ 0.2 ppb. Phys. Rev. Lett. **83**, 4510–4513 (1999)
74. G. Werth, J. Alonso, T. Beier, K. Blaum, S. Djekic, H. Häffner, N. Hermanspahn, W. Quint, S. Stahl, J. Verdú, T. Valenzuela, M. Vogel, Highly charged ions, quantum electrodynamics, and the electron mass. Int. J. Mass Spectrom. **251**, 152 (2006)

75. B. Mount, M. Redshaw, E. Myers, Atomics Masses of ^{6}Li, ^{23}Na, ^{38,41}K, ^{85,86}Rb, and ^{133}Cs. Phys. Rev. A **82**, 042513 (2010)
76. A. Wicht, J.M. Hensley, E. Sarajlic, S. Chu, A preliminary measurement of the fine structure constant based on atom interferometry. Phys. Scr. **T102**, 82–88 (2002)
77. K. Pachucki, A. Czarnecki, U. Jentschura, V.A. Yerokhin, Complete two-loop correction to the bound-electron g factor. Phys. Rev. A **72**, 022108 (2005)
78. S.J. Brodsky, S.D. Drell, Anomalous magnetic moment and limits on fermion substructure. Phys. Rev. D **22**, 2236–2243 (1980)
79. D. Bourilkov, Hint for axial-vector contact interactions in the data on $e^+e^- \to e^+e^-(\gamma)$ at center-of-mass energies 192–208 GeV. Phys. Rev. D **64**, 071701R (2001)